The design and study of a vapor chamber fabricated via laser powder bed fusion

by

Christopher M. Bailey

B.S., Indiana Institute of Technology, 2019

A THESIS

submitted in partial fulfillment of the requirements for the degree

MASTER OF SCIENCE

Alan Levin Department of Mechanical and Nuclear Engineering
Carl R. Ice College of Engineering

KANSAS STATE UNIVERSITY
Manhattan, Kansas

2022

Approved by:

Major Professor
Dr. Scott M. Thompson

Copyright

© Christopher Bailey 2022.

Abstract

Laser Powder Bed Fusion (LPBF) was utilized to create aluminum alloy (i.e., AlSi10Mg) specimens for two related sets of experiments for this study. The first was a series of 5-mm-diameter support pillars with a fixed height of 5 mm containing varying filet angles and build orientations (i.e., 0˚, 10˚, 20˚, 30˚, 40˚, 50˚, and 60˚ from the normal surface) to determine their effects on surface roughness and water wettability. From experiments, anisotropic wetting was observed due in part to the surface heterogeneity created by the LPBF process. The powder-sourced AlSi10Mg alloy, typically hydrophobic, exhibited primarily hydrophilic behavior for build angles of 0˚ and 60˚, a mix of hydrophobic and hydrophilic behavior at build angles of 10˚ and 20˚, and hydrophobic behavior at 30˚, 40˚, and 50˚ build angles. Measured surface roughness, Ra, ranged from 5-36 µm and varied based on location. Build angles of 30˚ and 40˚ provided for the smoothest surfaces. A significantly rougher surface was found for the 50º build angle. This abnormally high roughness is attributed to the melt pool contact angle having maximal capillarity with the surrounding powder bed. Based on the wetting and roughness data from the support pillars a 100 x 100 x 10mm vapor chamber (VC) was created at a 45˚ printing orientation from the normal surface to provide a proof of concept for the additive manufacturing (AM) of multiphase heat spreaders and its corresponding thermal conductivity. From production, it was found possible to manufacture and successfully inject an AM VC with deionized and degassed water as a working fluid. From experiments, the results were inconclusive to successfully determine a thermal conductivity; however, the critical temperature conditions necessary to begin multiphase thermal dissipation were observed.

Table of Contents

List of Figures v
List of Tables viii
Acknowledgements ix
Dedication x
Preface xi
Chapter 1 - Introduction 1
Chapter 2 - Laboratory and Experimental Setup 6
2.1 Vapor Chamber Testing Station 6
2.2 Vapor Chamber Charging Station 13
Chapter 3 - Fluid Contact Angles on Additively Manufactured AlSi10Mg Samples of Various Printing Orientations 16
3.1 Specimen Design and Manufacturing 16
3.2 Experimental Methods 18
3.3 Results and Discussion 23
3.4 Conclusions 38
Chapter 4 - Design and Manufacture of AlSi10Mg Vapor Chamber 39
4.1 Specimen Design and Manufacture 39
4.2 Experimental Methods 47
4.3 Results and Discussion 52
4.4 Conclusions 60
References 61
Appendix A - Full Drawing Print of Vapor Chamber 67
Appendix B - National Instruments LABVIEW VI Block Diagram 71

List of Figures

Figure 1.1: (Left) Empty laboratory at Rathbone 2086; (Right) current state of lab. xi
Figure 2.1: Flanged termination used for heater in this study. 7
Figure 2.2: Experimental VC holding assembly used in this study. 8
Figure 2.3: Thermocouple locations on condenser side VC (units in inches). 8
Figure 2.4: a) NI DAQ b) Thermocouple adaptor board and plugs on side of testing station c) Thermocouple weld (left) and plug (right). 10
Figure 2.5: Exploded view of interior setup used in this study. 11
Figure 2.6: Diagram of testing station. 12
Figure 2.7: Side view of testing station 13
Figure 2.8: Vapor chamber charging station used in this study 15
Figure 3.1: a) Specimen design including pillars with various chamfer angles; b) investigated orientation/build angles, ϕ, and upskin and downskin surface definitions. All dimensions are in millimeters. Adapted from [Figure 1]; Copyright ASME [1]. 18
Figure 3.2: Schematic of contact angle measurement apparatus showing digital goniometer AM sample surface. Adapted from [Figure 2]; Copyright ASME [1]. 19
Figure 3.3: Example goniometer image of droplet on AM surface with solid-liquid contact angles labeled. Adapted from [Figure 3]; Copyright ASME [1]. 20
Figure 3.4: Pillar geometry and locations of images in Figs. a. (3.6) b. (3.7) c. (3.8) d. (3.9). Adapted from [Figure 4]; Copyright ASME [1]. 21
Figure 3.5: Distribution of contact angle measurements (whiskers denoting high, low and average values) for each investigated printing/orientation angle. The red (solid) line indicates 90º; the critical contact angle that separates hydrophobic (top side) and hydrophilic (bottom side) conditions. Adapted from [Figure 5]; Copyright ASME. Credit to Jordan Morrow for creating this graph [1]. 25
Figure 3.6: Microscopy images (side views) of the partially melted metal beads present along the sides of Pillar 1 on each specimen. Adapted from [Figure 6]; Copyright ASME [1]. 27
Figure 3.7: Microscopy images (side views) of pillar chamfer on specimen 1 (ϕ=0). Note that Pillar 1 has a chamfer angle of 30º, Pillar 2 = 25º, Pillar 3 = 20º, Pillar 4 = 15º, and Pillar 5

= 10º. Partially melted metal beads are present in large quantities on all chamfer sizes. Adapted from [Figure 7]; Copyright ASME [1]. 28
Figure 3.8: Side-view microscopy images of the flat upskin portion of each specimen. Adapted from [Figure 8]; Copyright ASME [1]. 31
Figure 3.9: Optical microscope images (aerial view) of the flat upskin portion of each specimen. Adapted from [Figure 9]; Copyright ASME. Credit to Emily Stallbaumer-Cyr for taking these images [1]. 33
Figure 3.10: Location of profilometer measurement path to determine a) average roughness for the right side of the pillar (dark blue line) and a defect on the left side of the pillar (light blue line) b) average roughness for the top surface. Adapted from [Figure 10]; Copyright ASME [1]. 34
Figure 3.11: Average roughness of the top horizontal surface and the right and left sides of the pillar for each build orientation. Adapted from [Figure 11]; Copyright ASME. Credit to Jordan Morrow for creating this graph [1]. 36
Figure 3.12: Average roughness for the a) left side of the pillar and a defect on the left side of the pillar b) right side of the pillar and a defect on the right side of the pillar for each build orientation. Adapted from [Figure 12]; Copyright ASME. Credit to Jordan Morrow for creating this graph [1]. 37
Figure 4.1: Isometric, external view of the manufactured vapor chamber. 40
Figure 4.2: Side view of 1/8” NPT charging port. 41
Figure 4.3: Side view of M3 evacuating port. 41
Figure 4.4: View of the bottom of the vapor chamber showing the features created by the addition of 42 circumferential channels and the surrounding trench. 44
Figure 4.5: Close up view of the filling pattern used to create the support/wicking structures. The distance between the centers of the closest pillars was no less than 2 mm (shown in red). The angle between each row of pillars and the side of channel closest to the corner was 30˚ (shown in blue). 44
Figure 4.6: Close up view of the pyramidal geometry used in the meshing structure on the top of the vapor chamber. 45
Figure 4.7 Vapor Chamber Charging Setup 48
Figure 4.8 Vapor Chamber Charging Setup 49

Figure 4.9: Fully insulated experiment with vapor chamber pre-installed. 50
Figure 4.10: Experimental results for a 300W experiment. The x-axis is the time in minutes while the y-axis is the temperature in degrees C. 53
Figure 4.11: a) Average steady-state condenser side temperature. b) Average steady-state heater side temperature. c) Change in temperature during transient temperature state. 57
Figure 4.12: Experimental results for a charged 350W experiment. The x-axis is the time in minutes while the y-axis is the temperature in degrees C. 59

List of Tables

Table 1: Experimental contact angle measurements for 7 build orientations showing right and left contact angles. Adapted from [Table 1]; Copyright ASME [1]. 24

Table 2: Average steady-state temperatures for the vapor chamber at various power inputs. The percent change value is the average difference between the charged and empty experiments. All temperature values are in units of °C. 55

Table 3: Difference in temperature between the condenser and heater-side thermocouples at various power inputs. The percent change value is the average difference between the charged and empty experiments. All values are in units of °C. 55

Acknowledgements

I would like to acknowledge the other graduate students and undergraduate lab assistants which have helped me significantly over the past 3 years of research. The graduate students who have helped me most impactfully are Jordan Morrow and Emily Stallbaumer-Cyr who aided in experiments and results shown in Chapter 3 as part of a journal publication. The undergraduate lab assistants who have helped me most impactfully are Christian Reid, John Matulis, Cameron Weeks, and Zach Shultz who assisted in designing and constructing the lab equipment described and used throughout this study. I would like to thank Dr. Derby and Dr. Eckels for being a part of my thesis committee and providing very helpful insight throughout the course of this study. Lastly and most importantly, I would like to thank Dr. Thompson for the opportunity to study and learn under his guidance throughout the course of my master's degree. The following study would not have been possible without his direction and leadership.

Considerable portions of Chapter 3, "Fluid Contact Angles on Additively Manufactured AlSi10Mg Samples of Various Printing Orientations" have been paraphrased and directly cited from the ASME Journal of Manufacturing Science and Engineering Volume 144, which was written by myself and several previously mentioned students and professors in January 2022. I would like to acknowledge the ASME for permitting me to use this information in my thesis. Figures and Tables that have been adapted from this source are referenced according to their respective number in the journal publication. The citation to this journal article can be found in the references section of this thesis [1].

Dedication

I would like to dedicate this thesis to my loving friends and family who have constantly supported and prayed for me throughout out my pursuit of a master's degree. I would also like to dedicate this thesis to my wife, who has been instrumental in supporting me through a turbulent transition in life.

Preface

There are two studies that this thesis is founded on. The first study was conducted and submitted to the *ASME Journal of Manufacturing Science and Engineering* and contains excerpts and figures from Conference Paper SHTC2021-63599 which was peer reviewed and presented at the *ASME ES 2021 Summer Heat Transfer Conference*. The second study was conducted and presented in both *Research and the State 2020* and in the *Solid Freeform Fabrication Symposium 2021*. The data obtained from the first study were used to make design and manufacturing decisions in the second study.

Upon my arrival to K-State at the beginning of my master's degree, my advisor Dr. Thompson had also just recently arrived. The laboratory that we began research in was completely empty apart from a few desks and chairs. As shown in Figure 1.1, the lab is now filled with useful equipment and tools. The process of starting my research without any tools or equipment presented a unique and exciting challenge to overcome.

Figure 1.1: (Left) Empty laboratory at Rathbone 2086; (Right) current state of lab.

Chapter 1 - Introduction

The drive to create more powerful, yet increasingly small energy sources, has led to an issue of excessive heat flux in electronics packaging. High heat transfer within a concentrated area can result in electrical components overheating and/or warping. One solution to this problem is the use of a multi-phase heat spreader (i.e., thermal ground plane) such as a vapor chamber (VC) which effectively spreads heat within a hermetically sealed hollow chamber (or cavity) using a working fluid and wicking structures [2, 3]. Vapor chambers utilize fluid phase change to create temperature and pressure differentials, thereby promoting liquid and vapor slug movement throughout the cavity [4]. The design of a VC is somewhat limited in its geometrical complexity due to limitations in conventional manufacturing (e.g., end-milling, casting, etc.) and the need to integrate vacuum-grade joints to ensure hermetic sealing. In addition, wicking structures, which may exist as microchannels, sintered particles, or meshes, require cumbersome integration methods. With the use of layer-by-layer fabrication offered through additive manufacturing (AM) methods, such as Laser Powder Bed Fusion (LPBF), VCs with more complex geometric features are now possible [5,6].

Laser Powder Bed Fusion is an AM process commonly used for 'printing' metals. It uses a concentrated laser for selectively melting and fusing regions of a pre-deposited powder bed [7]. A thin layer of powder, approximately 30 μm in the case of this study, is evenly spread across a build plate; subsequently, the laser melts select regions corresponding to a solid model path, and once the entire cross-sectional area of the part has been fused, another layer of powder is evenly applied on top of the previous layer. This process is repeated until the part has been completed.

There are several design parameters associated with LPBF. The orientation and location of the part during printing will influence the surface parameters such as roughness, porosity, and

mechanical properties of the final structure [8]. One such study observed that the printing orientation of LPBF AlSi10Mg deviated the R_a value of surfaces by as much as 5 μm, thus in some cases, creating stress concentrations leading to an over 50% reduction in fatigue strength [9]. Furthermore, unmelted powder within any channels and/or cavities within the part must be removed after LPBF.

The benefits of using AM to produce complex VC geometries include being able to design and manufacture optimized and/or conformal designs with as-printed wicking structures more easily and cost effectively. In the study by Liu et al. [10] on the performance of VCs designed to mimic plant leaves, the process used to create the complex geometries ranged from chemical etching to graphite molding. The channel and wick designs employed were found to significantly improve heat transfer efficiency; however, the time and cost to produce such designs utilizing traditional manufacturing make scaled production of such VCs challenging. An experimental investigation was performed on a loop heat pipe with an additive-manufactured stainless steel primary wick cooling an 80-watt streetlamp. The heat transfer rate of the AM wick was 10% higher than a conventional wick loop heat pipe [11]. A porous regularly-patterned stainless steel wick structure created using selective laser melting technology was studied for its effective thermal conductivity, contact angle with multiple fluids (i.e., water, hexane, and ethylene glycol), and capillary performance. The wick showed improved capillary performance compared to sintered, mesh, or composite wicks; the large permeability was noted as the reason for the improved performance [12, 13]. A study conducted on the design of cooling layers for manufactured tooling determined that producing complex lattice structures via AM reduced cooling times within the cooling layers by 26% over a comparable design made utilizing traditional manufacturing methods [14]. Another

study conducted on the feasibility of producing an oscillating heat pipe with Ti-6Al-4V found a 500% increase of thermal conductivity over a solid titanium alloy [15].

Within a heat pipe, it is important to understand the surface roughness and the wetting phenomena because of their direct effects on heat transfer. The effects of surface roughness in natural convection play a major role in heat transfer. It was found that by modifying the surface from a 'smooth' to a 'rough' surface with 9 mm pyramids improved the circulation within a fluid chamber such that it increased thermal transport by 76%. It was also found that a change in surface roughness increased the number of 'thermal plumes' which were responsible for enhanced heat transport [16].

The surface roughness also impacts the contact angle. The contact angle of a droplet affects the surface area of the liquid on a solid surface, which in turn effects the rate of heat transferred to the liquid. The rate of evaporation, and therefore heat transfer, has been found to change depending on how a liquid droplet interacts with a surface. Contact angles directly affect the thin film thickness of the liquid which is where the majority of evaporation heat transfer occurs [17]. For water, contact angles which are less than 90˚ (i.e., hydrophilic) generally have linear evaporation rates, whereas contact angles which are greater than 90˚ (i.e., hydrophobic) typically have non-linear evaporation rates [18]. The contact angle of water on AM AlSi10Mg is considered hydrophobic [19]. Contact angles in the context of VCs are most affected by heat transfer rate, solid heat transfer properties, liquid/gas heat transfer and fluid dynamics properties, surface roughness, internal surface geometries, and surface treatment. A droplet sitting on a surface will be in one of two states – Cassie or Wenzel [20]. In the Cassie state, the droplet sits on top of the microscale ridges of the surface typically on pockets of air; in the Wenzel state, the droplet sits inside the microscale ridges of the surface and is pinned to the surface. Typically, when a surface

is hydrophobic, increasing surface roughness will make the droplet more hydrophobic, and when a surface is hydrophilic, increasing surface roughness will make the droplet more hydrophilic. Both hydrophobicity and hydrophilicity have their advantages for heat transfer. In condensation, a hydrophobic surface sheds droplets faster to keep the liquid film resistance lower, thereby increasing heat transfer [21, 22]. In boiling, a hydrophilic surface is advantageous to maintain a layer of liquid water on the heated surface, thereby minimizing the effect of dryout [23].

Several recent studies have focused on understanding the process-structure-property relationships inherent to the LPBF of AlSi10Mg. In particular, process parameters such as laser power and laser beam diameter have been found to have a significant effect on AM surface quality [24, 25]. Many of these studies have revealed important surface roughness features for this specific alloy.

In general, the LPBF process can yield a lot of variations in properties such as surface roughness and porosity due to the nature of the melting and solidification process [26]. Processes can be taken to change the surface conditions with coatings [27], remelting [28, 29] and adding microstructures [30, 31] which can have a great effect on fluid contact angles. Parts made via LPBF are prone to having a surface roughness that varies along their perimeter – based on how that perimeter is oriented with respect to the build direction. Surface portions that are facing upward are ‘upskins’ while surface portions facing downward, toward the substrate, are ‘downskins’ [32]. Upskin surfaces are typically smoother, due to there being more solidified material underneath them and gravity pushing the melt pool to spread along the surface more, while downskin surfaces are typically rougher as they interact more with the powder bed where capillary forces pull on the melt pool during processing.

This first half of this thesis aims to determine the effects of printing orientation on surface roughness and fluid contact angles for as-printed LPBF AlSi10Mg surfaces. The relationship between the LPBF AlSi10Mg surface and surface wetting has not received significant attention in the literature. In the studies conducted herein, uncoated, untreated surfaces were characterized since this would be a typical surface condition in many heat pipes due to its cost savings. This study also seeks to provide insights on surface roughness and fluid wetting behavior that will be present in such multi-phase thermal heat spreaders.

The second half of this thesis, utilizing the results of the surface wetting study, aims to provide a proof-of-concept for an additively manufactured vaper chamber fabricated from AlSi10Mg. This study observed the manufacturing, processing, and charging of a novel vapor chamber as well as the observation of thermal dissipation. The lessons learned from this study may benefit the design considerations of future additively manufactured multi-phase thermal heat spreaders.

Chapter 2 - Laboratory and Experimental Setup

2.1 Vapor Chamber Testing Station

The laboratory supplies and experimental equipment required for vapor chamber filling, sealing and characterization were assembled. Two experimental stations, a heat pipe testing station and heat pipe charging station, as well as the necessary supplies and infrastructure were purchased for the laboratory. In order to conduct the experiments required for this study, a custom heat pipe testing/characterization station was created which needed to accomplish several essential goals including:

1. Determine the heat transfer rate/thermal conductivity of various heat pipes
2. Provide and measure effective heat input on the bottom side of various heat pipes
3. Provide and measure effective cooling input on the top sides of various heat pipes
4. Measure the surface temperatures in multiple locations across various heat pipes
5. Obtain surface temperature measurements at various orientations
6. Provide effective insulation for experiments to minimize heat loss

To provide the heat input for this study, a Barry 800W thermal test vehicle chip with flanged termination was connected to a DROK AC 110V to DC 0-48V converter adjustable AC-DC transformer max 480W power supply which can be seen in Figure 2.1. The power supply operated at 10A and could be adjusted from 0-48V. The flanged termination and its soldered connections were very fragile and needed to be built into a more solid assembly which can be seen in Figure 2.2. To provide the cooling input for this study, a PolyScience LM61GX1A110C 1/3 HP benchtop chiller with a maximum pump rate of 7.9 l/min and a temperature range of -10°C to 30°C was filled with purified water and connected to the experimental setup. The setup, which was designed to maintain laminar flow, included a Custom Thermoelectric WBA-4.0-0.92-CU-01 101.6 x 101.6

x 23.5mm (4” x 4” x .92”) copper water block connected to the benchtop chiller with high-pressure tubing. The temperature and volumetric flow rate of the water was measured with a Picomag flow meter after the water flow had been reconnected on the other side of the experiment. For this study, the temperature of various locations across the vapor chamber was measured using 13 type-T thermocouples (±1 °C resolution) which, on the condenser side, whose welded tips were held in the locations shown in Figure 2.3 by a 101.6 x 101.6 x 4.75mm (4” x 4” x 3/16”) copper plate with 8-1.58mm (1/16”) channels. Each thermocouple tip was located at the end of these channels. The channels were oriented to center and provide stability for the condenser-side thermocouples. On the heater side, the thermocouples were placed on the VC 15mm from each edge of the flanged termination heater and held in place with heat resistant tape and adhesive.

Figure 2.1: Flanged termination used for heater in this study.

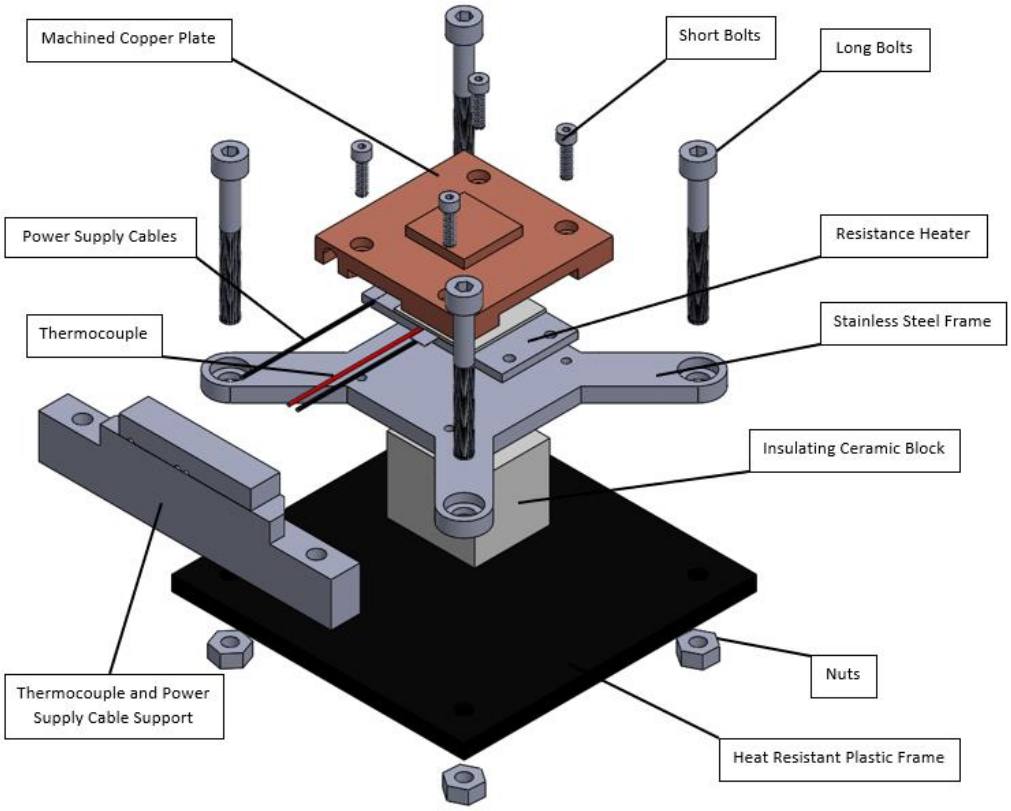

Figure 2.2: Experimental VC holding assembly used in this study.

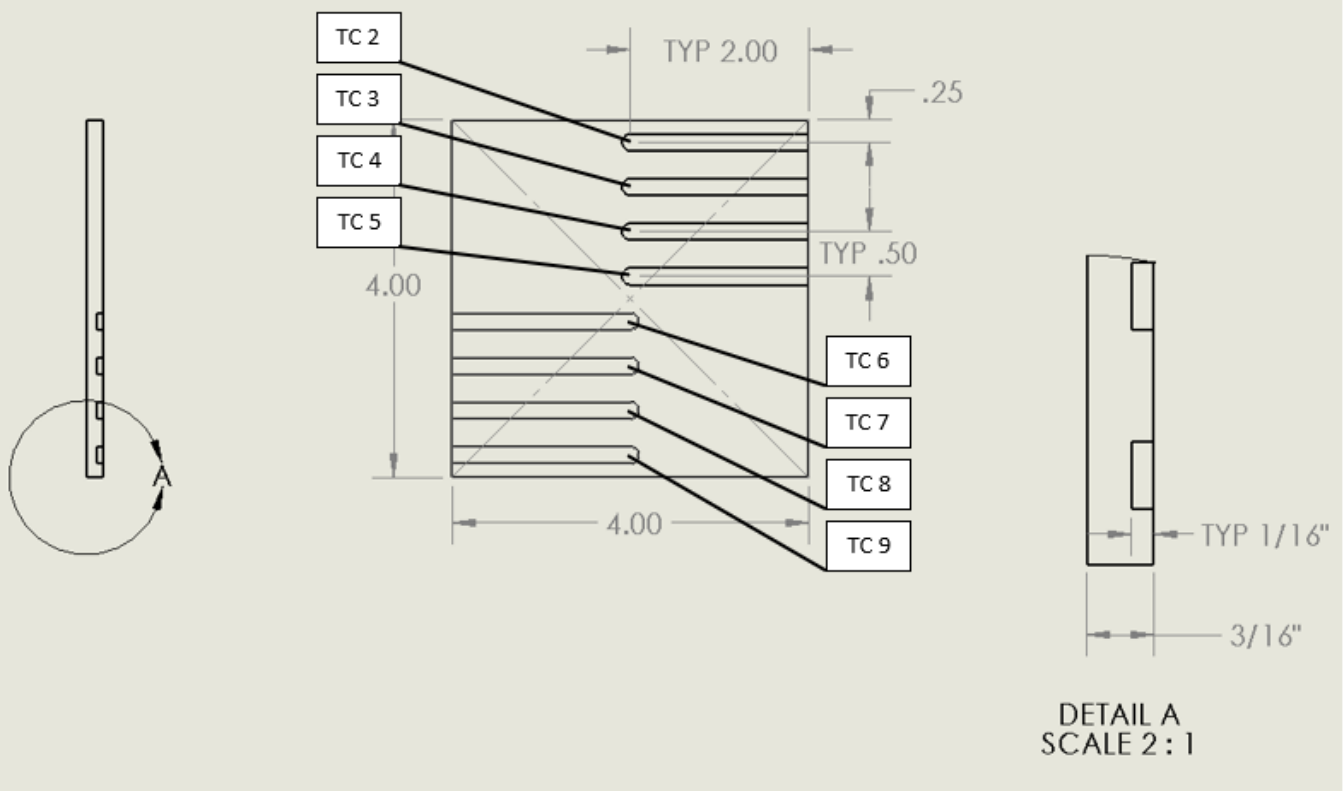

Figure 2.3: Thermocouple locations on condenser side VC (units in inches).

The thermocouples were in this specific orientation to determine the heater temperature, the difference in temperature between the top and bottom of the VC (in the z-axis), and the difference in temperature across the top of the VC (in the x/y-axis). Thermocouple 1 was placed on the inside of the heater as shown in Figure 2.2. Thermocouples 2-9 were placed across the condenser side of the VC water cooling block. Thermocouples 10-13 were placed 15 mm from the walls of the heater assembly along the midpoint axes. There were more thermocouples placed on the top of the VC than the bottom because it was less difficult to orient and maintain their location throughout the study. All 13 thermocouples were connected to a National Instruments cDAQ-9174 which can be seen in Fig 2.4. To make the thermocouples easier to use, two thermocouple adaptor boards and type-T thermocouple plugs were placed on the side of the experimental setup. These adaptor boards and plugs made it possible to interchange or replace faulty thermocouple tips into different DAQ channels without having to rewire the entire setup.

a)

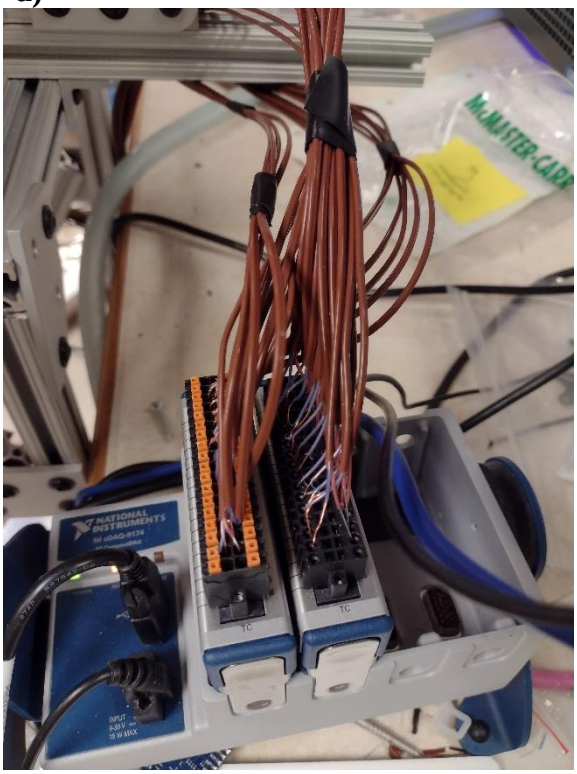

b)

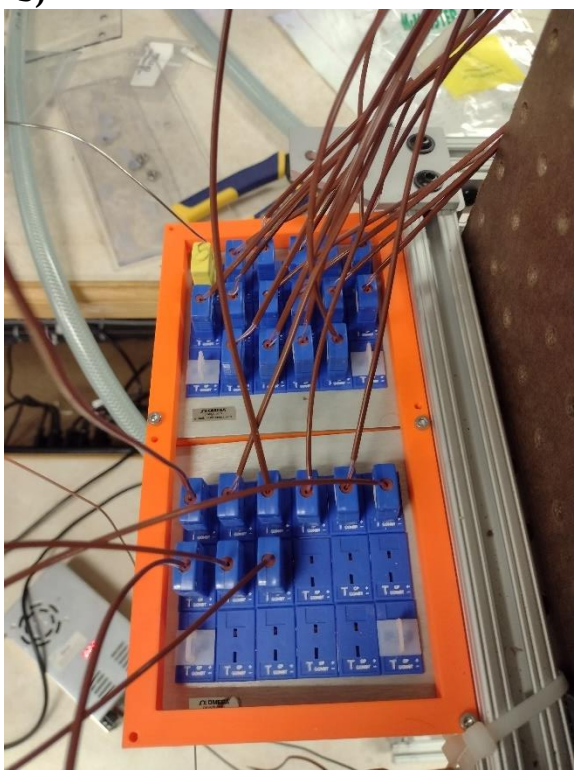

c)

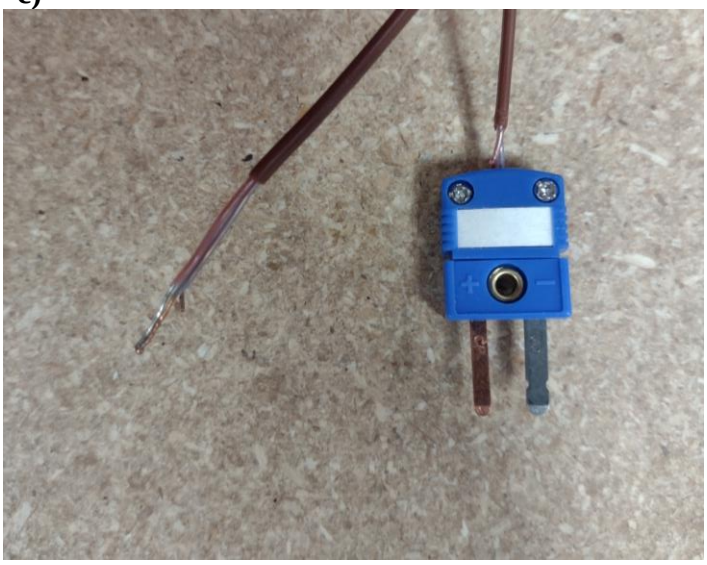

Figure 2.4: a) NI DAQ b) Thermocouple adaptor board and plugs on side of testing station c) Thermocouple weld (left) and plug (right).

For the experimental setup, the previously mentioned components were all stacked together such that the heater assembly was applying a heat flux to the bottom of the VC and the copper water block was removing heat on the top of the VC. The copper plate was placed between the VC and the water block. The heater and water block's orientation were intentional so that gravity would assist with the evaporation/condensation cycle on the interior of the VC. All thermally significant surfaces had a coat of thermal paste (Omegatherm 201 High Temperature & High Thermally Conductive Paste) to it prior to experimentation. The exploded view of the internal setup can be seen in Fig 2.5 and the exterior of the testing station can be seen in Fig 2.6.

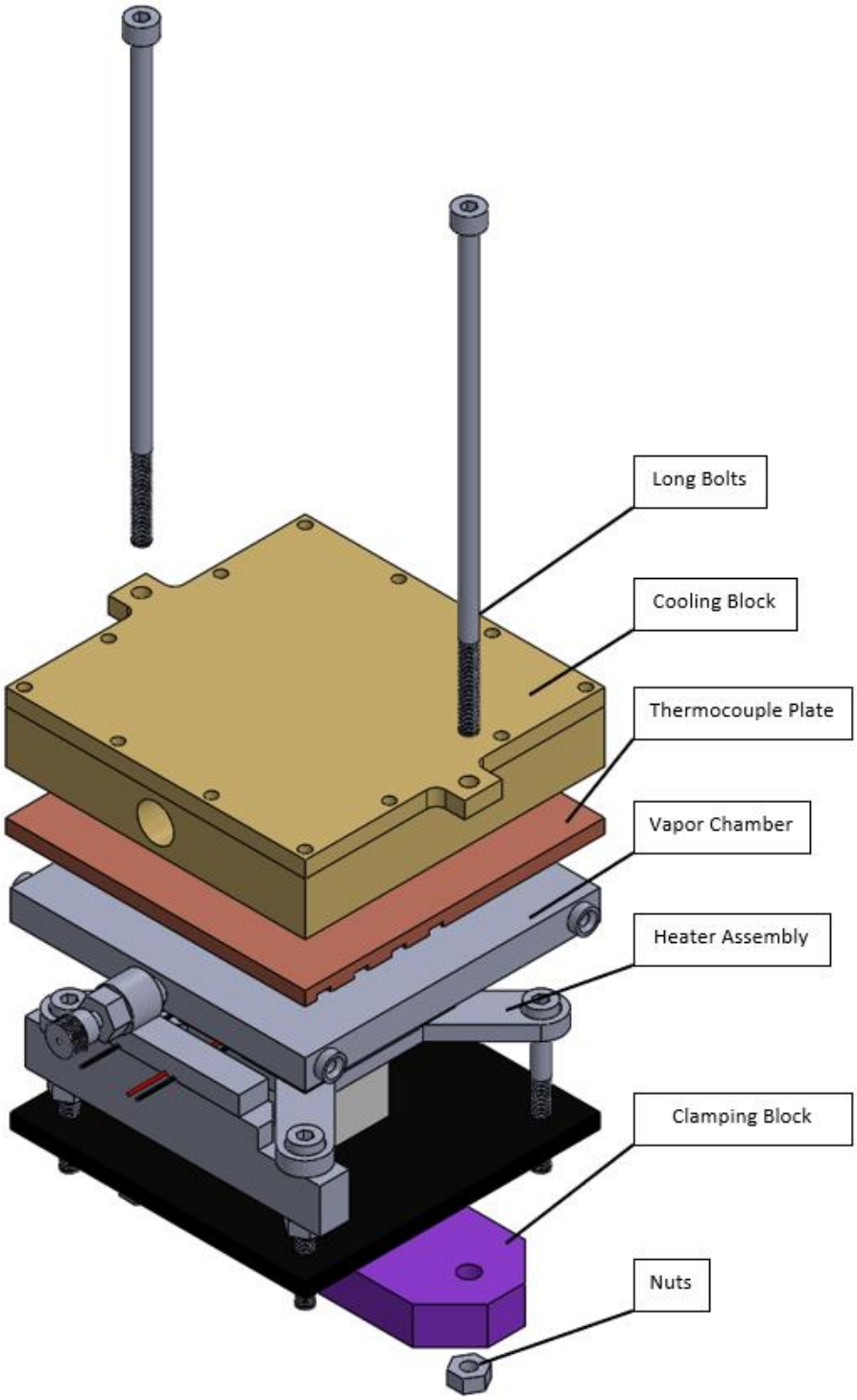

Figure 2.5: Exploded view of interior setup used in this study.

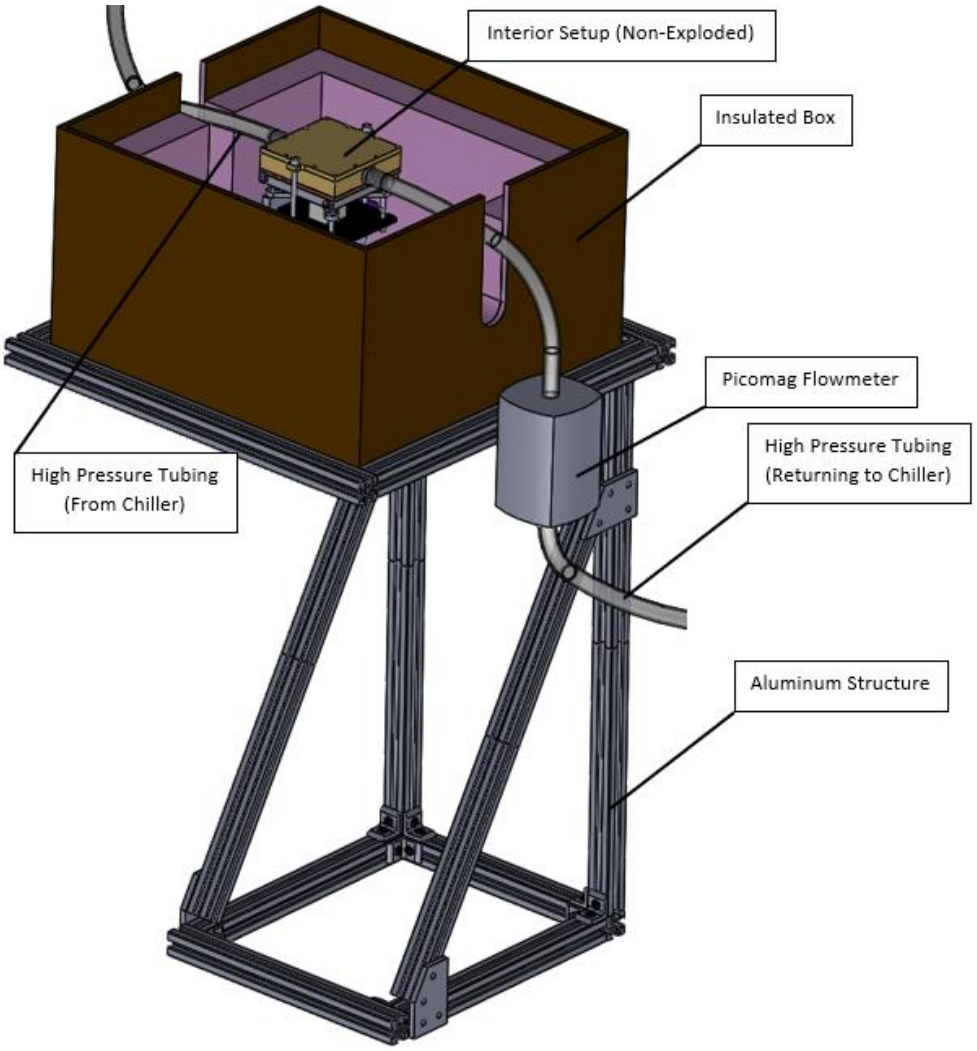

Figure 2.6: Diagram of testing station.

In order for an experiment to be run at different VC orientations, the testing station was designed to raise and lower about an axis on the back of aluminum structure. The testing stand was held in place by running high strength braided polyethylene cord from the front of the insulated box through a system of pullies on ceiling of the laboratory and down again to a lockable hand crank. The testing stand could be oriented from horizontal to a 90˚ angle. The angle which the testing stand was oriented could be measured by a digital level oriented parallel with the bottom surface of the VC. The side view of how the testing station could be oriented can be seen in Fig 2.7.

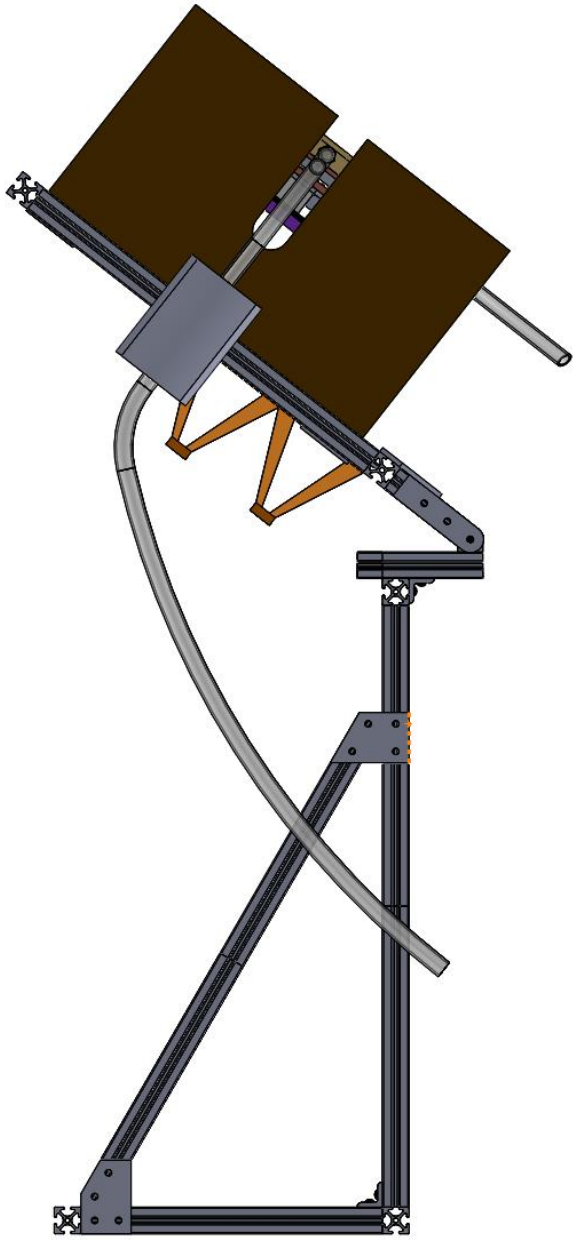

Figure 2.7: Side view of testing station

2.2 Vapor Chamber Charging Station

A properly manufactured VC contains specific amount of a working fluid which will both evaporate and condense under vacuum pressure. The manufacturing process required to inject the

VC with this working fluid is called 'charging'. In order to properly charge the VC, the following requirements were necessary for a VC charging station:

1. Air inside of VC must be evacuated and vacuum pressure must be obtained
2. Degassed-deionized water must be injected into VC
3. Filling level inside of VC must be accurately known
4. Upon successful charge, VC must remain hermitically sealed
5. VC must be able to be re-charged at different fill ratios

To achieve these requirements, a VC charging station shown in Fig 2.8 was constructed which both charged the VC as well as degassed the deionized water which was used as working fluid. The system, measured by a digital pressure gage, was held under vacuum pressure using a vacuum pump capable of holding pressure as low as $1x10^{-4}$ Torr. The vacuum pump was protected from contaminants by an in-line liquid nitrogen cold trap. The cold trap was connected to the first of three Swagelok valves which could be independently opened and closed to allow specific parts of the experimental setup to be brought to vacuum pressure. The second valve was connected to a vacuum grade 500 mL beaker which could be inserted into a heated ultrasonic shaker bath to degas the working fluid. The beaker set on a 3D printed flask holder to ensure it did not come into contact with the side of the heated ultrasonic shaker. Upon a successful degassing procedure, the flask could be removed from the bath and tipped to pour working fluid into the VC. The third valve was connected to a 1/16" copper tube which connected directly into the VC. The VC sat on an Ohaus EX1103 high-resolution (±0.001g) enclosed scale during the charging process to observe the amount of fluid that was being injected into it. The high-pressure tubing which connected to the VC was connected to a secondary Swagelok valve which was held level to the scale to ensure that the weight of the copper and tubing did not affect the weight of the VC. Once the desired

amount of fluid had been injected into the VC, the Swagelok valves could be closed, and a hydraulic crimper could be used to hermetically seal the 1/16” copper tube.

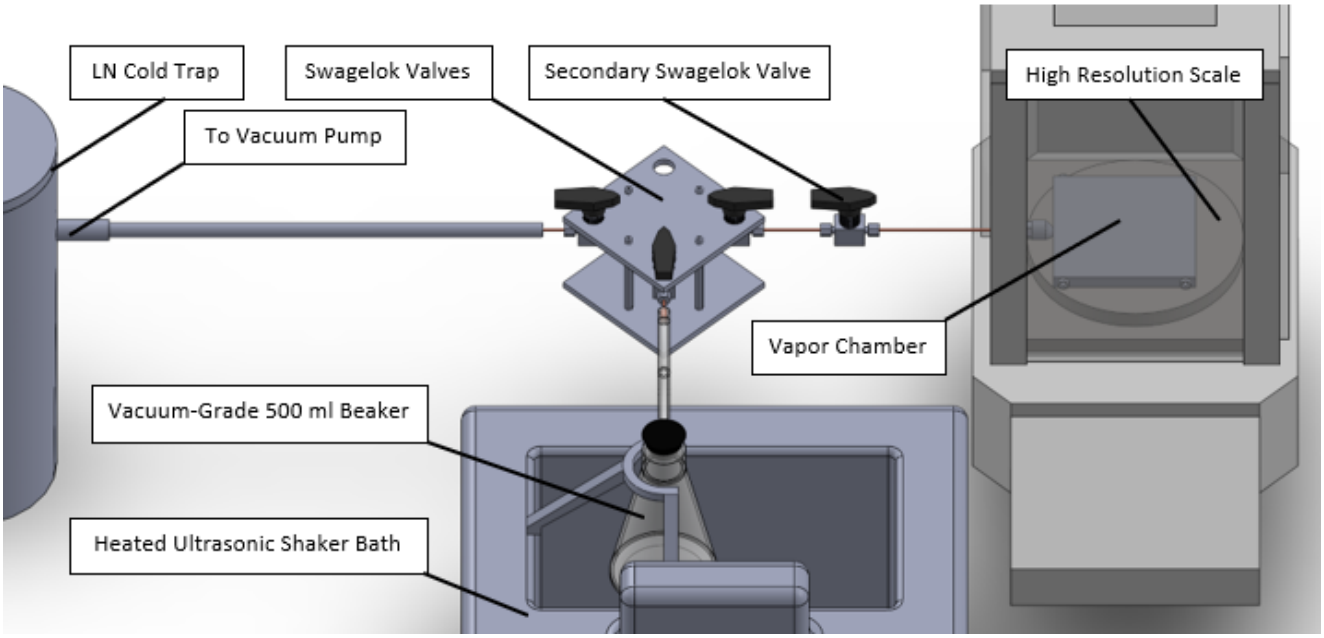

Figure 2.8: Vapor chamber charging station used in this study

Additional laboratory equipment including a Prusa MMU 3D printer, Form 3 resin 3D printer, soldering station, and thermocouple welding station were purchased and utilized throughout this study.

Chapter 3 - Fluid Contact Angles on Additively Manufactured AlSi10Mg Samples of Various Printing Orientations

3.1 Specimen Design and Manufacturing

Specimens were fabricated via LPBF using spherical AlSi10Mg (cast aluminum alloy) powder (i.e., 10-45 μm normally-distributed diameters) as the raw material. This specific alloy was chosen due to its additive manufacturability, low cost, and relatively high thermal conductivity [33]. Although copper is the typical material-of-choice for thermal management media, it is a considerably more expensive material to manufacture via LPBF. It is also a much denser material making it less viable in applications requiring low weight thermal solutions. Currently, the processing of copper alloys via LPBF is still in development and not widespread. Hence, the use of LPBF of aluminum thermal management devices is of interest and the focus of this current study. The LPBF of all specimens were fabricated using LPBF services provided by Protolabs. Each layer was set to a thickness of 30 μm, providing for high resolution with tolerances of ± 0.1 mm. The specimens were manufactured with a GE Concept Laser M2 using a 370 W Nd:YaG fiber laser with a spot size of 200 μm and a scan speed of 1800 mm/s. The material composition, whose exact material composition and density were proprietary, were provided as follows: Al (87.1-89.35 weight %), Si (9-11%), Fe (0.55%), Cu (0.05%), Mn (0.45%), Mg (0.2-0.45), Ni (0.05), Zn (0.1), Pb (0.05%), Sn (0.5%), Ti (0.15%). Because the thermal properties, specifically the melting point, of each material are unique it can be assumed that the resulting material is anisotropic [34, 35].

Seven specimens with dimensions shown in Figure 3.1 were printed, each with its own build orientation/angle, ϕ (i.e.: 0˚, 10˚, 20˚, 30˚, 40˚, 50˚, and 60˚) normal to the build plate surface. All specimens had the same design consisting of 5-mm tall pillars with 5-mm diameters for

potential use inside a VC. Such pillars provide chamber support and provide another means for mass and heat transfer via wicking [36]. Five pillar geometries with chamfer angles of 30˚, 25˚, 20˚, 15˚, and 10˚, were created to determine if there were significant effects on surface roughness with a change in printing angle. The specimens were printed with the flat surface opposite the pillars as the base; meaning, the pillared surface was the 'upskin' of the part during LPBF. Apart from the pillar geometries, there was space on the upskin of the specimen which was intention6ally left flat to measure the surface roughness and contact angles which may represent VC surfaces within the cavity. As shown in Figure 3.1, when changing the build angle, the orientation angle of the pillars changed. This effect on the upskin and downskin (identified in Figure 3.1) surface roughness was investigated through microscopy of the pillar profiles.

Prior to any measurements, the specimens were rinsed with isopropyl alcohol, acetone, then water and then allowed dry. This cleaning process represents one used to clean and remove excess, entrapped metal powder from within a cavity of a VC manufactured via LPBF. Specimen surfaces were not coated in order to better represent the surfaces of as-printed, internal geometries. The typical procedure for the removal of excess metal powder within an internal geometry is to implement sealable ports into the side of the specimen, which enables it to be rinsed [15].

a)

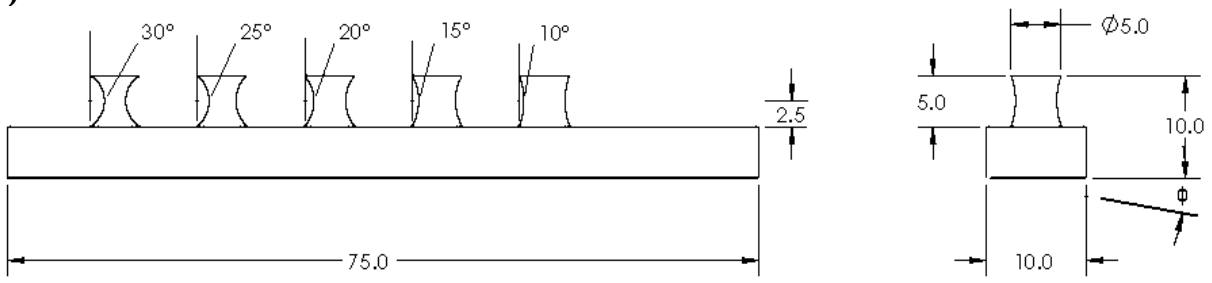

b)

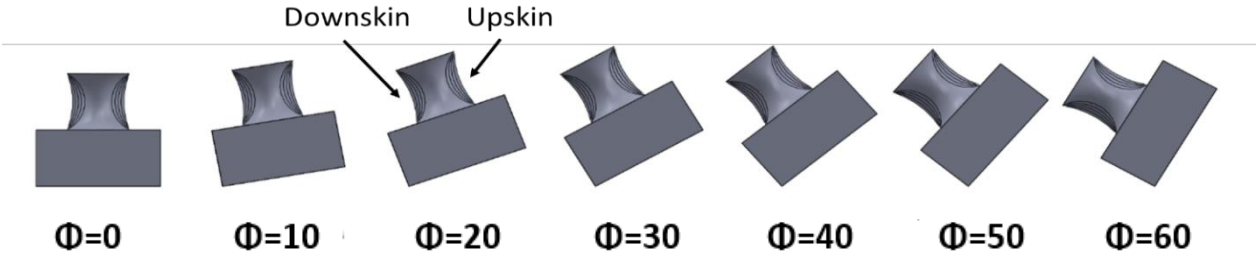

Figure 3.1: a) Specimen design including pillars with various chamfer angles; b) investigated orientation/build angles, ϕ, and upskin and downskin surface definitions. All dimensions are in millimeters. Adapted from [Figure 1]; Copyright ASME [1].

3.2 Experimental Methods

To characterize the relationship of surface roughness and contact angles with build orientation of the AlSi10Mg specimens, two experiments were conducted. The first experiment aimed to determine the solid-liquid, initial contact angle, θ, with a 0.2 μL (± 0.08 μL) deionized water droplet on the flat portion of the upside of each specimen. The contact angle of the water droplet was measured using a digital goniometer (Allied Prosilica GC model # GC750 using the software FTA 32), the contact angles were measured using Photon FastCam Viewer 4, and the results were exported to a Microsoft Excel spreadsheet for analysis (Figure 3.2). The droplet was placed by hand on the specimen surface with the Fisher Brand Elite Adjustable-Volume pipette oriented as vertical as the goniometer allowed; the surface temperature was monitored using a type-T thermocouple (±1 ºC resolution) resting on the same sample surface as the droplet. Contact angle measurements were done at room temperature, nominally 22 ± 1 ºC.

Once the 0.2-μL water droplet had ceased moving from being placed on the specimen's surface, achieving a steady-state morphology, a picture (640x480 96 dpi) was taken which enabled the solid-liquid contact angle to be calculated by the digital goniometer software. The droplets would remain in a steady-state morphology for several minutes on the surface of the specimen at room temperature before completely evaporating. The contact angles of three water droplets

placed in different locations on the flat surface of each specimen were measured by the digital goniometer, for a total of 42 contact angle measurements. The contact angles of both the left and right side of the two-dimensional water droplet image were obtained, and an average contact angle calculated from both the left and right contact angles was obtained from each droplet. The average contact angle of all three water droplets on each specimen was also calculated. An example image of a droplet with contact angle measurements obtained via the goniometer can be seen in Figure 3.3. Note that the small weight of the droplets prevented any gravity influence on droplet morphology as shown by its Bond number, Bo, being much less than unity (details later discussed).

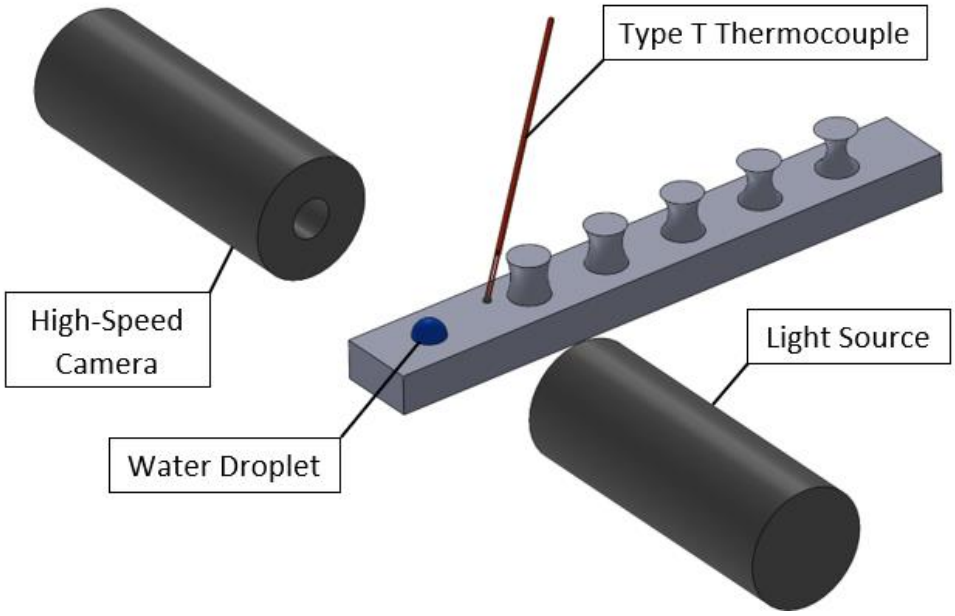

Figure 3.2: Schematic of contact angle measurement apparatus showing digital goniometer AM sample surface. Adapted from [Figure 2]; Copyright ASME [1].

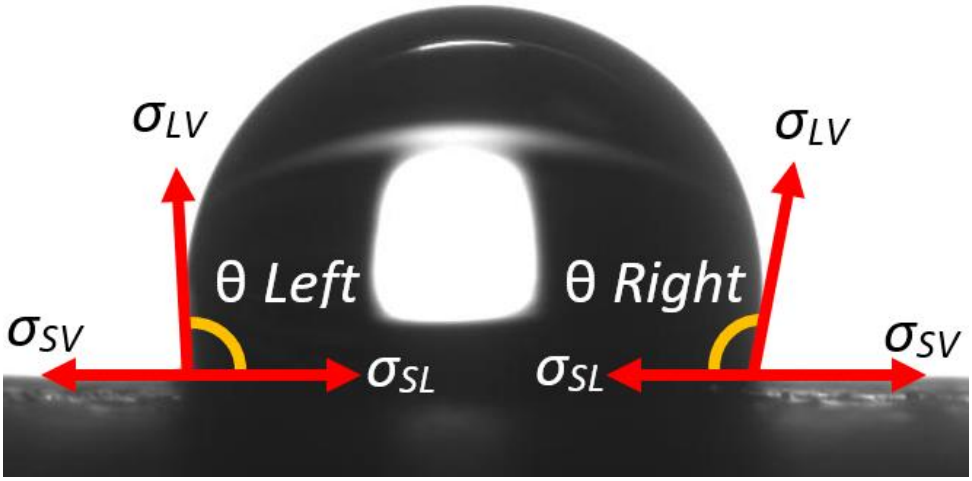

Figure 3.3: Example goniometer image of droplet on AM surface with solid-liquid contact angles labeled. Adapted from [Figure 3]; Copyright ASME [1].

The second set of experiments focused on determining the impacts that build orientation and pillar geometry had on surface roughness. Several images of each specimen were taken utilizing an optical microscope (Amscope ME520T) magnified 5x. Side and top view images were taken of each flat surface and while only side view images (at two different magnifications) were taken for each pillar. The sides of each pillar were observed with the optical microscope to determine upskin/downskin variation and whether a significant and observable difference in surface roughness was present between chamfer angles on the same specimens. The pillar roughness profiles are important since, once incorporated into the internal geometry of a multi-phase heat spreader, they act as wicking structures. Because a majority of evaporation takes place in the bridging area near the solid-liquid interface, the surface of these structures implies the wetting behavior of liquid droplets; and therefore, heat transfer. The flat surfaces were important to observe to determine whether a trend between printing orientation and surface roughness, and consequentially, liquid contact angles was present. Figure 3.4 shows the pillar geometry and location of the pictures taken with an optical microscope for the specimens throughout this study.

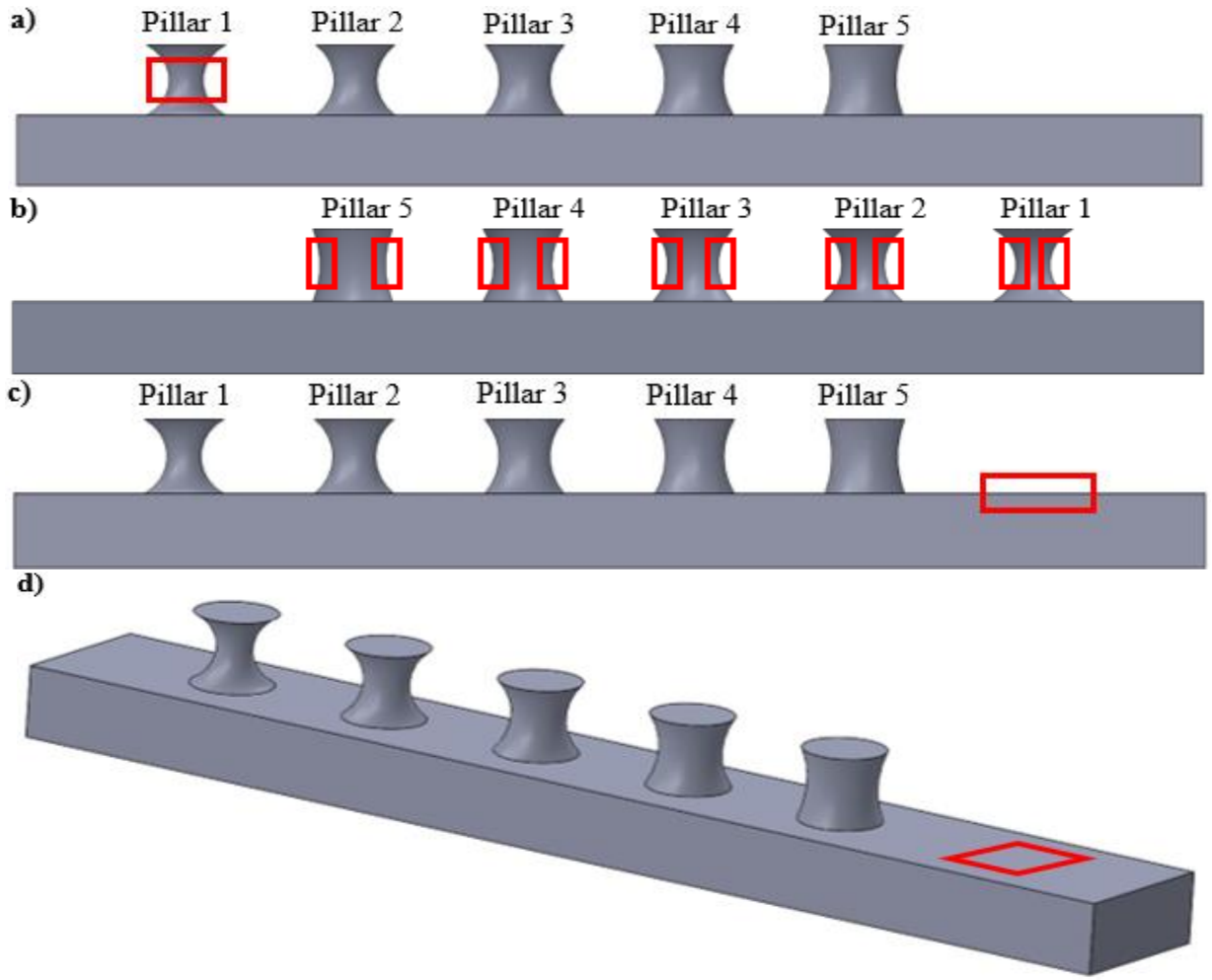

Figure 3.4: Pillar geometry and locations of images in Figs. a. (3.6) b. (3.7) c. (3.8) d. (3.9). Adapted from [Figure 4]; Copyright ASME [1].

Once images had been taken using the optical microscope, the specimens were cut into 6 pieces so that they could be observed under a scanning electron microscope (SEM). SEM microscopy was performed using a Low Vacuum SEM (Model: Carl Zeiss EVO MA 10) operating at 5 kV. Due to the specifications of the microscope, the specimens could not fit into the observation platform without first being separated. Each of the pillars, as well as the flat portion of the specimens, were separated from each other and rinsed to remove contaminants.

Specimens were then measured for surface roughness at 5 locations via an EDM MVi5 profilometer with FANUC 5-Axis software. A roughness measurement was taken along the flat surface of each part in the same location that contact angles were previously recorded. Two

different roughness measurements were taken on both the left (downskin) and right (upskin) sides of each 10˚ chamfer pillar. Theoretically, on the 0˚-built specimen, the downskin and upskin surface roughness values would be equivalent because their build orientation would be the same. One measurement was taken in a location with a large partially melted metal bead to obtain a value of high surface roughness and one measurement was taken in close proximity to this location such that there were relatively few partially melted metal beads. This was done on both the upskin and downskin sides of the pillars to obtain high and low surface roughness values to provide a more accurate surface characterization.

3.3 Results and Discussion

Contact angle measurements

A total of 42 initial contact angle measurements were recorded for the flat surface of each specimen and the results are shown in Table 1. To determine whether the values obtained in this study were statistically relevant, the parameter p-value was calculated using a single factor analysis of variance (ANOVA). The p-value of the contact angle measurements, which are shown in Table 1, was determined to be 0.001 which is less than the value 0.05 required to verify that the contact angle values obtained in this study were statistically relevant. AlSi10Mg alloy is typically hydrophobic [19]. However, data presented in Table 1 and Figure 3.5 indicate that the build angle, ϕ, influences wettability and subsequent contact angle, θ. Variation was observed between the left-hand-side and right-hand-side contact angles for most droplets, indicating some nonuniformities in surface roughness and composition due to the LPBF manufacturing process. For build angles of 0˚ and 60˚, contact angles indicate that the surface is primarily acting hydrophilicly, although the variance is larger for the 0˚ build angle. At build angles of 10˚ and 20˚, some droplets were hydrophilic on one side and hydrophobic on the other; it is possible that partially melted metal beads, as discussed in the following section, may contribute to this nonuniformity. For 30˚, 40˚, and 50˚ build angles, droplets consistently exhibited hydrophobic behavior and partially melted beads were smaller in diameter. It was observed that there was a higher amount of partially melted metal beads on the surface of the $\phi = 0^{\circ}$ specimen; upon contact with partially melted metal beads left over from the LPBF process, the water droplet would 'attach' itself via surface tension which greatly affected the contact angles [4,28,37]. As the printing angle increased, the surface became more water repellant until the experiments reached the fifth specimen (ϕ=40˚). It was observed that contact angle irregularity (left-hand-side and right-hand-side variation) generally decreased as

the build angle increased. These trends indicate that the surface roughness decreases as the build angle increases, which allows for more droplet stability.

Table 1: Experimental contact angle measurements for 7 build orientations showing right and left contact angles. Adapted from [Table 1]; Copyright ASME [1].

Build Angle	Contact Angle [°]			
	Left	Right	Avg	Tot Avg
Φ=0°	43.7	67.3	55.5	74.4
	77.9	82.0	79.9	
	81.7	93.6	87.7	
Φ=10°	108.4	86.0	97.2	96.2
	107.5	96.1	101.8	
	83.3	95.9	89.6	
Φ=20°	90.4	82.9	86.6	88.3
	89.2	89.2	89.2	
	83.5	94.8	89.2	
Φ=30°	98.4	101.5	99.9	100.8
	106.1	98.0	102.0	
	100.8	100.3	100.5	
Φ=40°	109.7	114.5	112.1	106.7
	107.9	110.7	109.3	
	96.8	100.6	98.7	
Φ=50°	102.3	103.0	102.7	100.6
	100.2	98.6	99.4	
	99.3	100.3	99.8	
Φ=60°	84.5	83.2	83.9	82.8
	81.5	82.0	81.7	
	83.4	81.9	82.7	

A pure liquid in contact with its own vapor atop a smooth solid while under steady-state conditions has a contact angle which is a function of its interfacial surface tension. An equation relating surface tension and contact angle is Young's equation which states:

$$\sigma_{LV}\cos(\theta) = \sigma_{SV} - \sigma_{SL} \quad (1)$$

where σ is fluid surface tension, θ is the solid-liquid contact angle, and subscripts *S*, *L*, and *V* stand for solid, liquid, and vapor, respectively. For static fluid wetting of rough horizontal surfaces,

Young's equation may be multiplied by roughness, γ, which is the ratio of the actual solid surface area, A_s, per unit of area projected on a horizontal plane, A_{hor}:

$$\gamma = \frac{A_s}{A_{hor}} \tag{2}$$

$$\cos(\theta) = \frac{(\sigma_{SV} - \sigma_{SL})}{\sigma_{LV}} \gamma \tag{3}$$

Per Young's equation, it is clear that roughness directly impacts contact angle. For a unity roughness, i.e. γ = 1, the contact angle is equivalent to that experienced on a smooth surface. For hydrophilic surfaces, roughness often decreases contact angle, whereas for hydrophobic surfaces, roughness can increase contact angle [38]. However, roughness alone is not sufficient to characterize a surface; these results demonstrate impacts of partially melted metal beads, which are nonuniform on the surface.

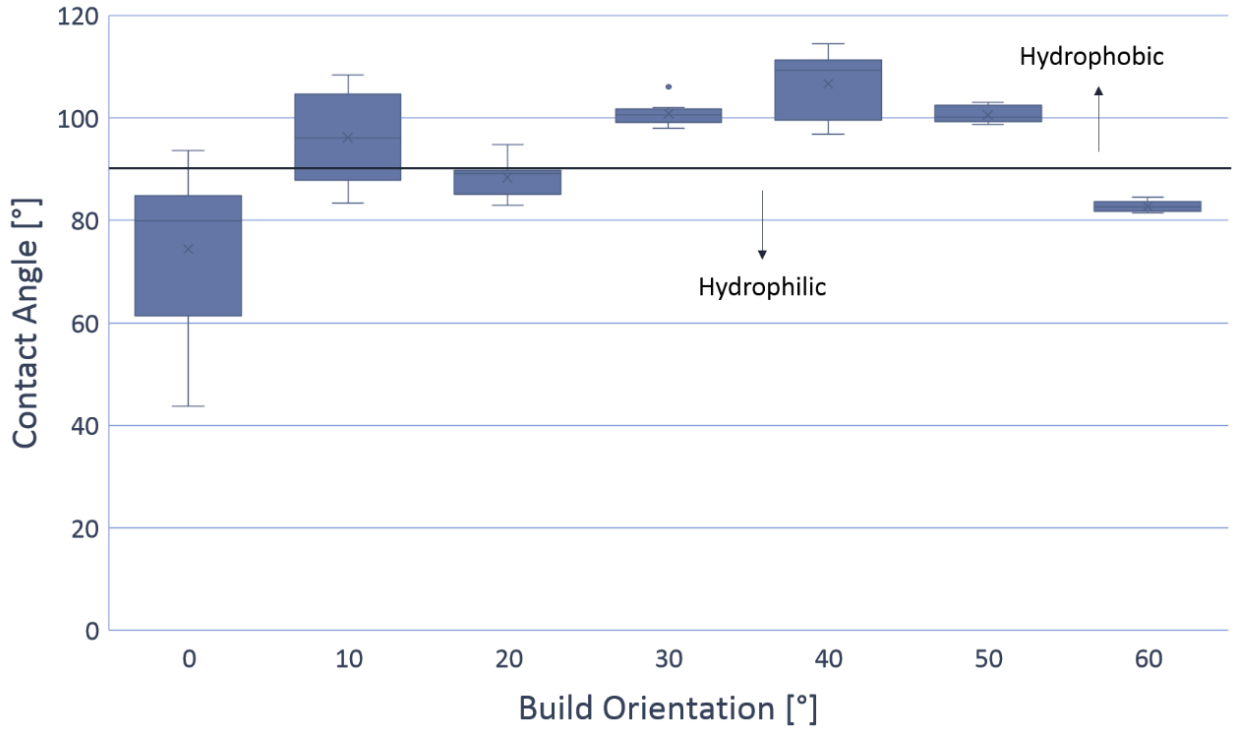

Figure 3.5: Distribution of contact angle measurements (whiskers denoting high, low and average values) for each investigated printing/orientation angle. The red (solid) line indicates 90°; the critical contact angle that separates hydrophobic (top side) and hydrophilic (bottom side) conditions. Adapted from [Figure 5]; Copyright ASME. Credit to Jordan Morrow for creating this graph [1].

Microscopy

Via optical microscopy, it was observed that the sides of the pillars along all seven specimens contained a considerable amount of partially melted beads. Per Ref. [24], the ratio between laser power and laser beam diameter, P_L/d_b, used in the LPBF of AlSi10Mg parts was optimum in the range of 3000 W/mm < P_L/d_b < 3500 W/mm. Values lower than 2000 W/mm generally led to the creation of partially melted metal beads and uneven roughness values [24]. For this study, P_L/d_b = 1850 W/mm, and this explains the excessive formation of partially melted metal beads on the specimens in this experiment. However, in the context of VCs, a large surface area and a rough texture may in fact benefit heat transfer and bubble formation during fluid phase change [39]. Images of the partially melted metal beads on the pillars are shown in Figs. 3.6-3.10.

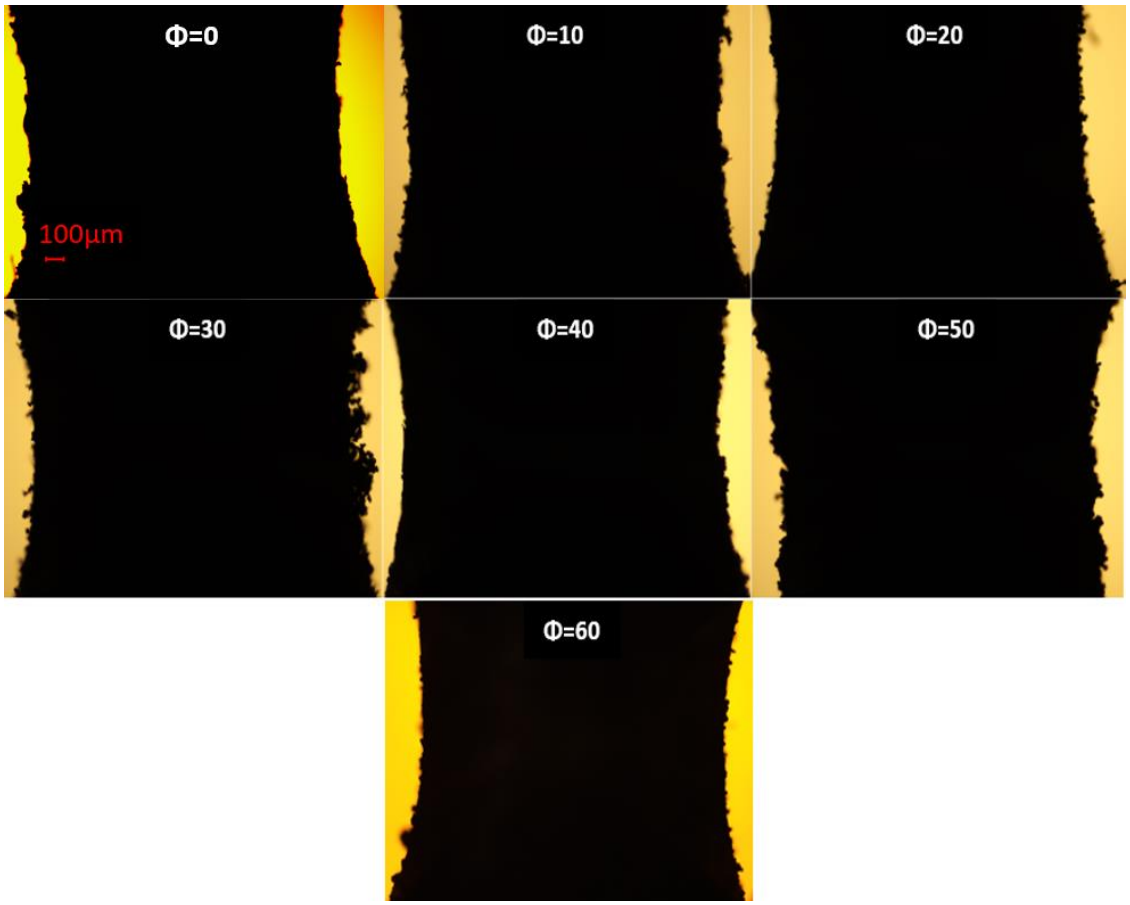

Figure 3.6: Microscopy images (side views) of the partially melted metal beads present along the sides of Pillar 1 on each specimen. Adapted from [Figure 6]; Copyright ASME [1].

a) *Pillar 1*

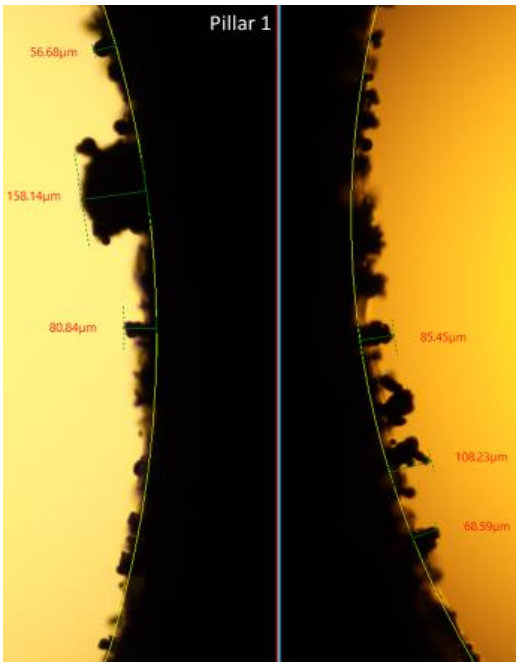

b) *Pillar 2*

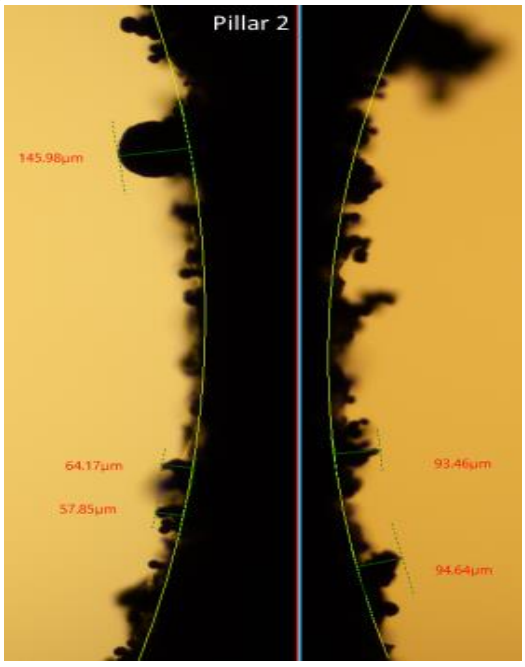

c) *Pillar 3*

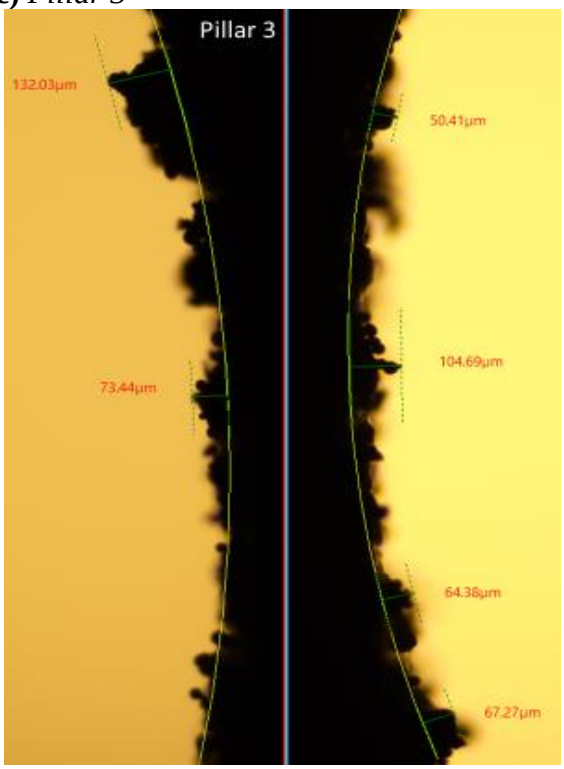

d) *Pillar 4*

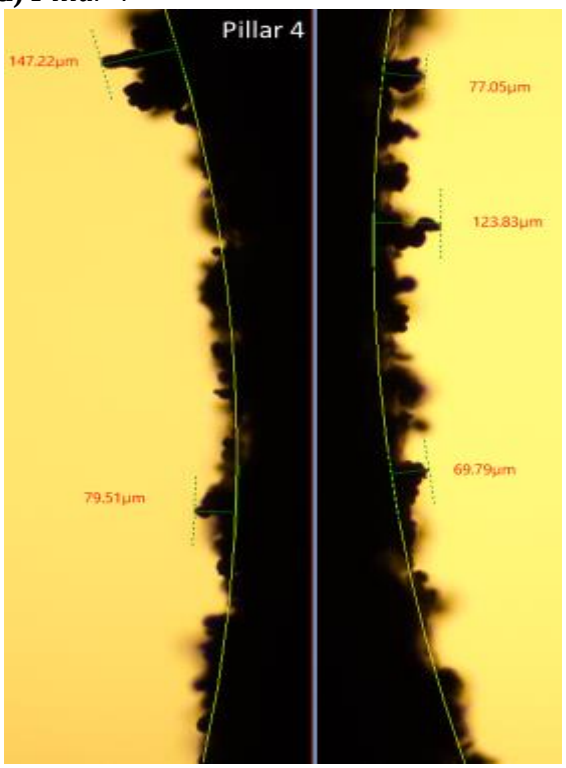

e) *Pillar 5*

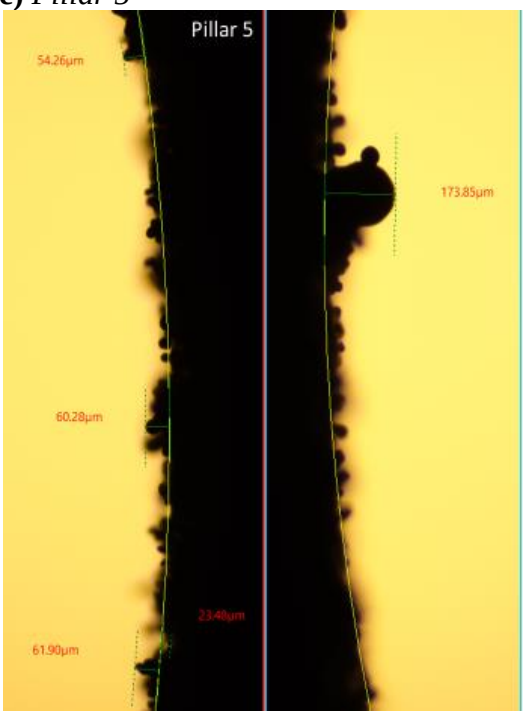

Figure 3.7: Microscopy images (side views) of pillar chamfer on specimen 1 (ϕ=0). Note that Pillar 1 has a chamfer angle of 30º, Pillar 2 = 25º, Pillar 3 = 20º, Pillar 4 = 15º, and Pillar 5 = 10º. Partially melted metal beads are present in large quantities on all chamfer sizes. Adapted from [Figure 7]; Copyright ASME [1].

In Figure 3.7, the shared downskin/upskin sides of Pillar 1 are visible. These are the sides that are visualized when looking directly at an upskin or downskin. It is interesting to note that the shared downskin/upskin sides are smoothest for the 40º and 60º build orientations, while roughest for the 30º and 50º build orientations. For Figure 3.7, note that Pillar 1 has a chamfer angle of 30º and Pillar 5 has a chamfer angle of 10º, with each pillar chamfer angle in between varying by 5º (see Figure 3.1a). From Figure 3.7, it may be seen that partially sintered beam widths varied from ~20 µm to as high as 174 µm. Agglomerations of powder with satellites are evidenced in Figure 3.7a and 3.7d-e indicating that the chamber angle had little-to-no influence on agglomeration. There is no clear trend between pillar chamfer angle and surface roughness. However, it does appear that the steepest chamfer angle of 10º provided for the smoothest surface with the exemption of the lone agglomeration along its right side. All other chamfer angles provided for pillars with profound agglomeration – more pronounced and sporadic than that observed for Pillar 5 (10º chamfer angle).

The flat upskin surface (non-pillared) of each part was observed from two different angles, from the side and from the top, (Figure 3.8 and Figure 3.9). There was a trend in partially melted bead size; as the printing angle increased, the bead size generally decreased. Partially melted beads were most prominent for low build angles and diameters reduced with increasing build angle. This, in the context of how the specimens were printed, makes sense as the effect of gravity would pull these beads to the side, rather than leave them standing upright [40]. For the horizontally-printed specimen, the flat upskin was found to have one of the largest attached particles in this study, at 234 µm. The surfaces without partially-sintered particles were found to have numerous ‘mounds’ indicating a some type of balling effect taking place during LPBF. Figure 3.9, which is a top view of the flat portion of the specimens, continues to show how gravity perpendicularity affects the

LPBF melt pool and subsequent surface features. Surface roughness variability, as well as a few partially melted metal beads which have formed because of the AM process, can be seen in these figures. The flat surface of specimen 5 (ϕ=40) was the smoothest. It had the smallest difference in height and had relatively fewer partially melted metal beads. This corresponds directly with the contact angle observed earlier and explains the trend in increasing water repellency as the printing angle approached 40º. Parallel track lines are visible in Figure 3.9; however, they become less apparent as the build angle increases, especially for those greater than 40º. The white and yellow streaks present in Figs. 3.8-3.9 are the result of the lighting required to obtain high resolution images of the specimens.

a) ϕ=0º

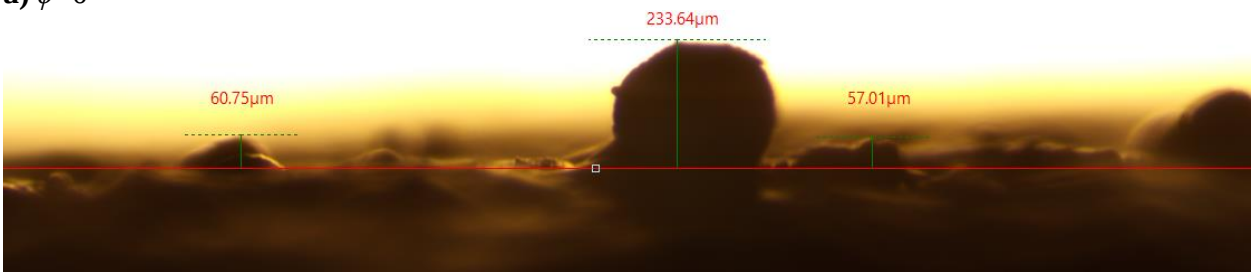

b) ϕ=10º

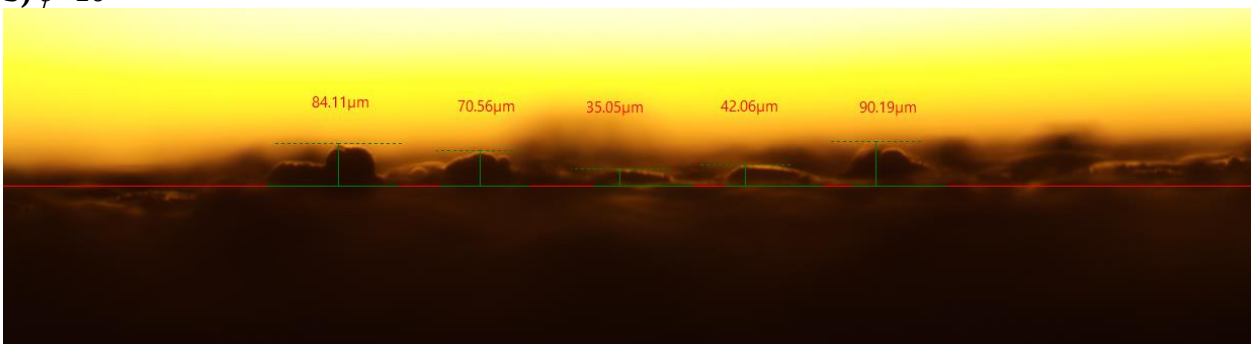

c) ϕ=20º

d) ϕ=30º

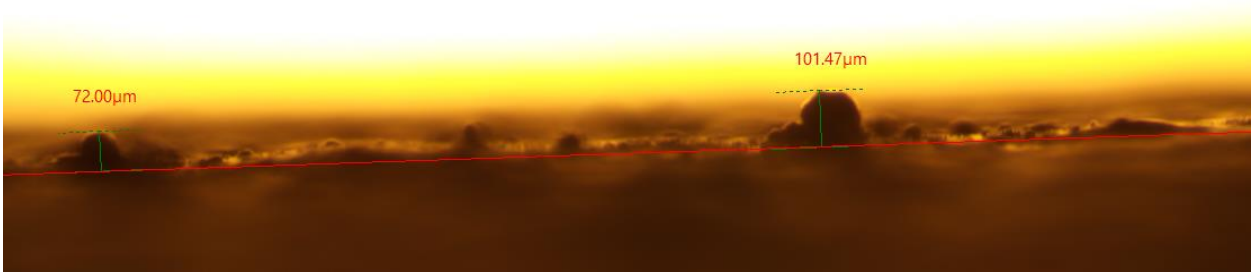

e) ϕ=40°

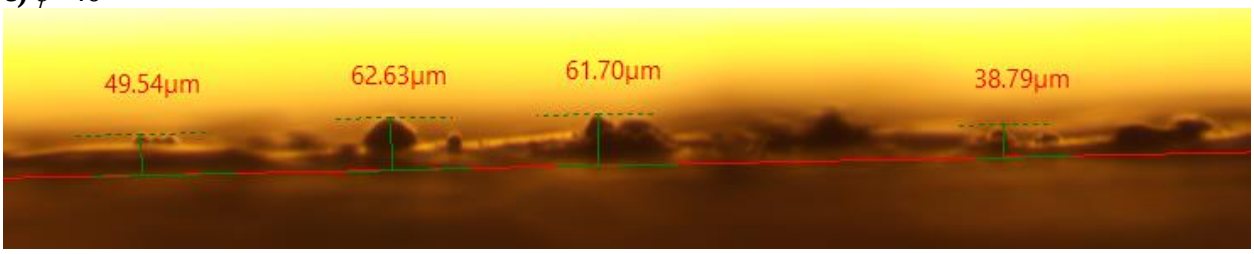

f) ϕ=50°

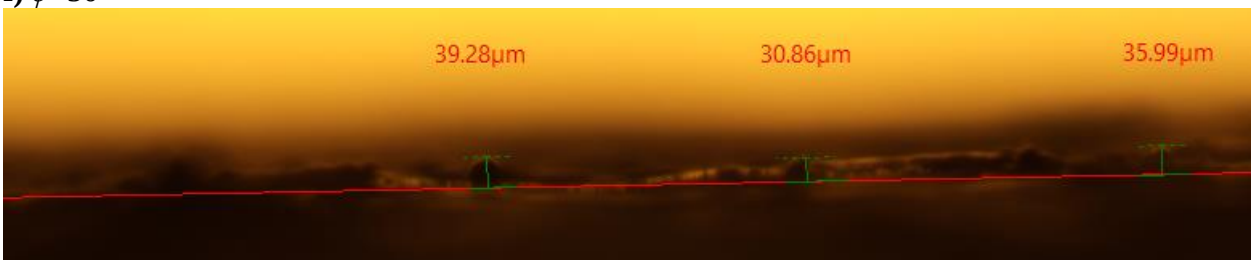

g) ϕ=60°

Figure 3.8: Side-view microscopy images of the flat upskin portion of each specimen. Adapted from [Figure 8]; Copyright ASME [1].

a) ϕ=0^o

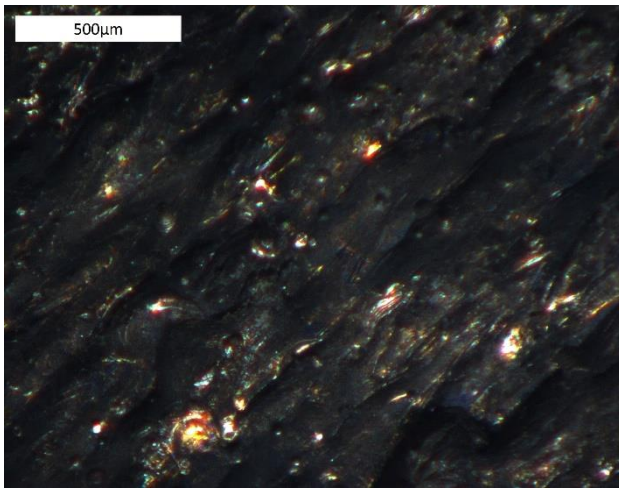

b) ϕ=10^o

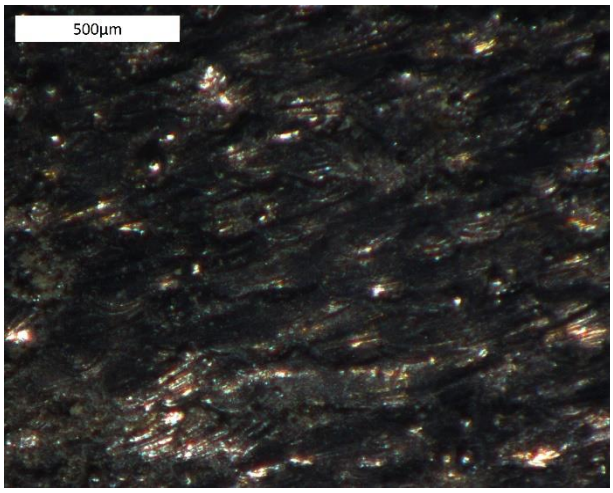

c) ϕ=20^o

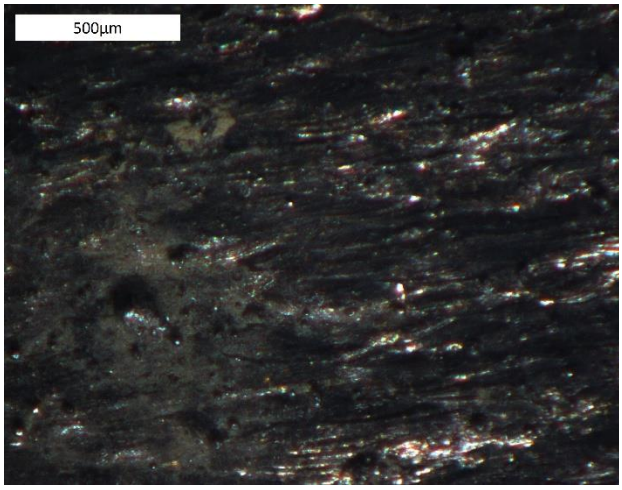

d) ϕ=30^o

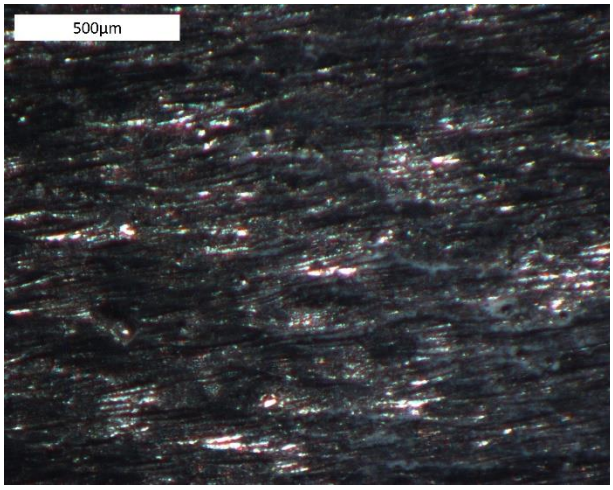

e) ϕ=40^o

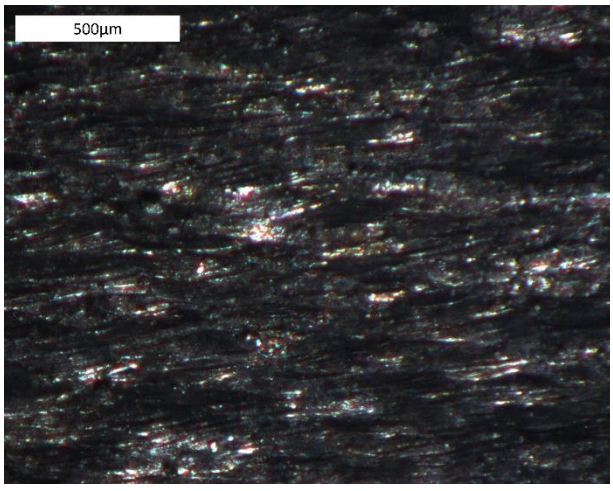

f) ϕ=50^o

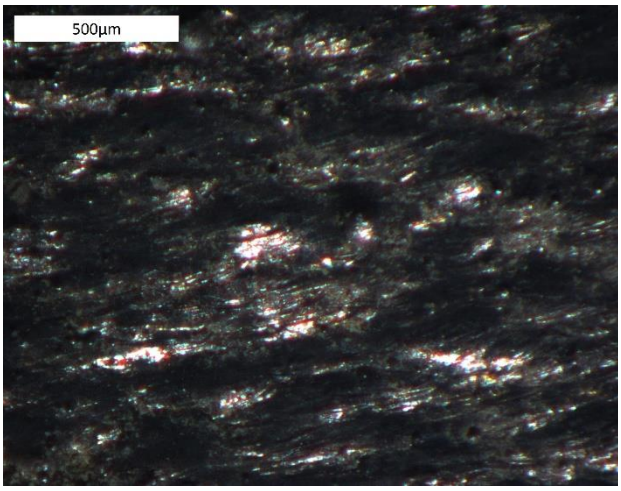

g) ϕ=60^o

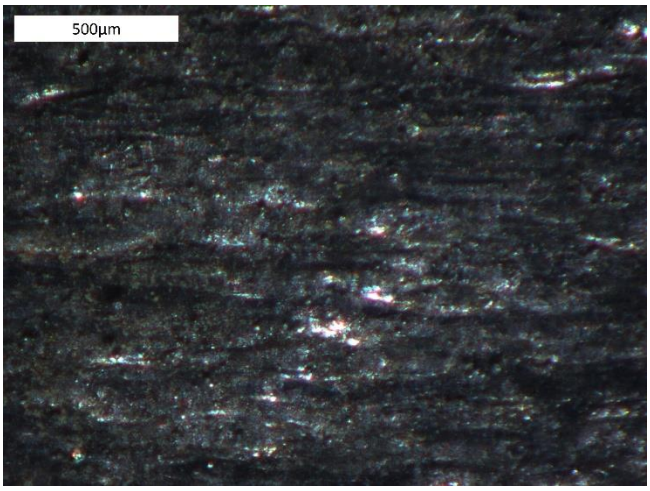

Figure 3.9: Optical microscope images (aerial view) of the flat upskin portion of each specimen. Adapted from [Figure 9]; Copyright ASME. Credit to Emily Stallbaumer-Cyr for taking these images [1].

Profilometer measurements

As shown in Figure 3.10, profilometer measurements were performed to obtain five average roughness values, R_a, along various locations of the specimens. One measurement was obtained from the flat upskin portion of the part in the same location that the contact angle measurements were previously obtained (Figure 3.11) and four measurements were obtained along the sides of the pillars (Figure 3.12). The pillar roughness measurements were taken on both the left and right sides of the pillar corresponding to their upskins and downskins during LPBF, respectively. Note the evidence of localized burning along the pillar shown in Figure 3.10 occurring along a shared upskin/downskin side.

a)

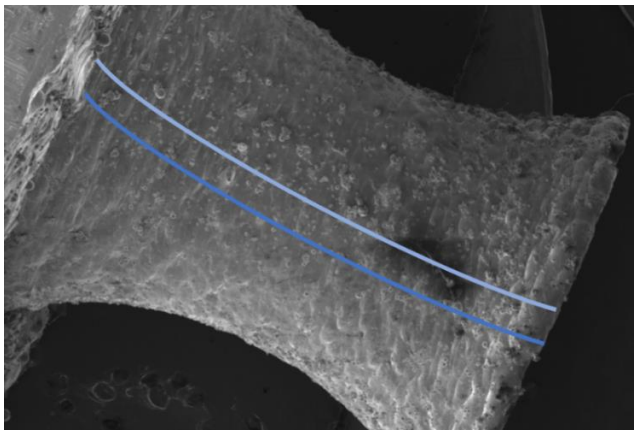

b)

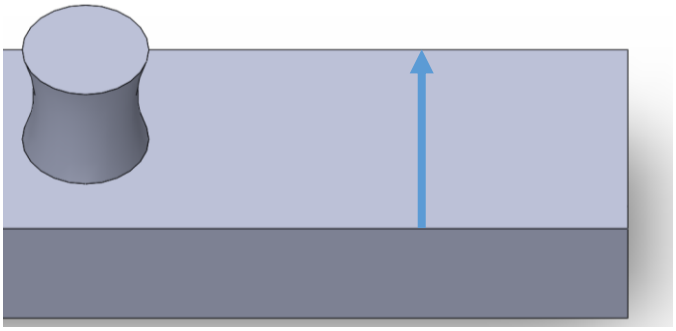

Figure 3.10: Location of profilometer measurement path to determine a) average roughness for the right side of the pillar (dark blue line) and a defect on the left side of the pillar (light blue line) b) average roughness for the top surface. Adapted from [Figure 10]; Copyright ASME [1].

As shown in Figure 3.10, the upskin profilometer measurements were averaged over a path 8.25 mm in length while the pillar profilometer measurements were averaged over a path 4.15 mm in length along their height. From Figure 3.11, the upskin (left side) surface of each pillar was found to possess average roughness values between 8.04-12.4 µm whereas the downskin (right side) surface had average roughness values between 9.25-17.6 µm. The upskin and downskin surface roughnesses of the investigated pillars clearly depend on build angle. In all cases, and as expected, the upskin surface of the pillar was smoother than its downskin surface. This is attributed to the downskin being surrounded by unmelted powder which acts as a thermal insulator and wicking medium, causing the melt pool to run hotter and be 'pulled' upon, respectively. The upskin has the advantage of having solid metal beneath it to help conduct heat away. In addition,

the gravity force depresses the melt pool more due to the underlying solid preventing any permeation, generally resulting in smoother profiles. Significantly more variance in roughness was found for the pillar downskin relative to its upskin. A maximum roughness near 18 μm was measured for the pillar downskin on the 50º-built specimen. The 0º, 10º, and 60º-built specimens possessed pillars with downskin roughness values between 12-14 μm. The smoothest pillar downskins were found for the 20º, 30º, and 40º-built specimens, ranging between 9-12 μm. The upskin surface roughness values of the pillar generally increased with specimen build orientation. The upskin surface was smoothest for the 0º and 10º build orientations with values near 7-8 μm. The results demonstrate an inflection point in upskin and downskin surface roughness values – occurring around a specimen build orientation of 50º. The upskin surface roughness of the specimen flat region was highest for the 0º build orientation (~16.5 μm) and generally became smoother as the build orientation increased, being approximately 5 μm at the 60º build orientation. The trend is broken for the 50º build orientation, in which the upskin surface roughness of the specimen's flat region is higher than that for the 40º build orientation. The upskin surface roughness barely changed for build orientations between 20º and 40º.

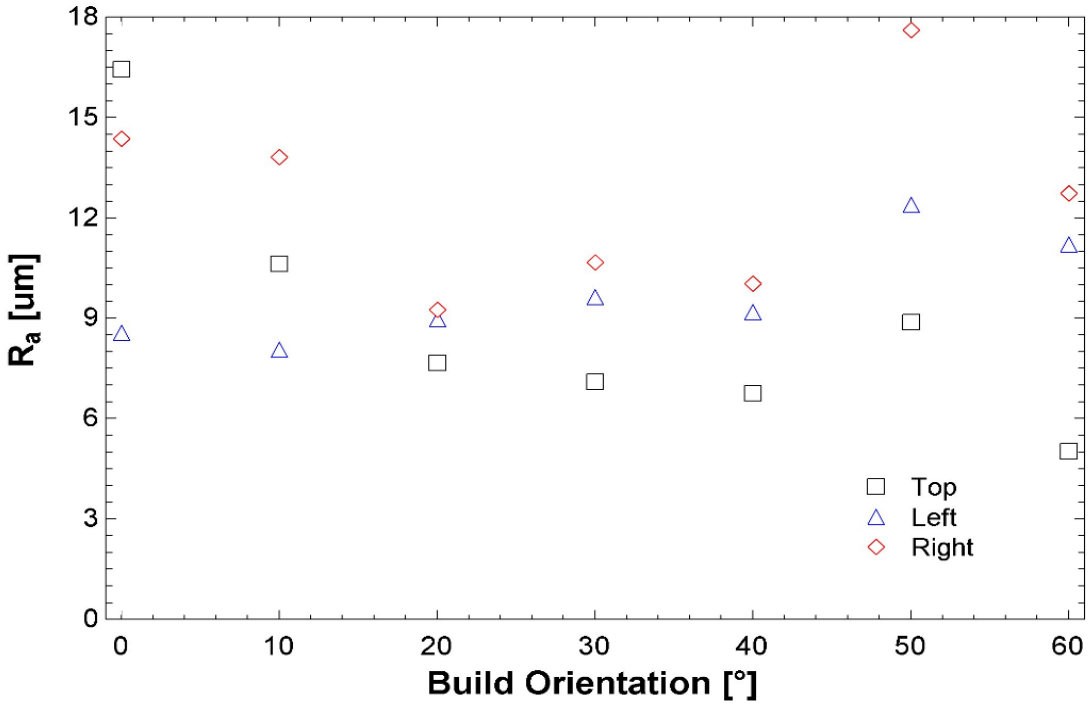

Figure 3.11: Average roughness of the top horizontal surface and the right and left sides of the pillar for each build orientation. Adapted from [Figure 11]; Copyright ASME. Credit to Jordan Morrow for creating this graph [1].

The roughness values for notable partially-attached beads (defects) on the upskin (left) and downskin (right) portions of the investigated pillar are shown in Figure 3.12. It may be seen that there is strong variance in defect roughness, ranging between 11-38 µm for the pillar upskin and 12-27 µm for the pillar downskin. The defect roughness appears to have no relationship with build orientation due to the random powder size distribution used during LPBF. The variance in defect roughness is less for the pillar downskin and this may be attributed to powder bed capillary effects.

a)

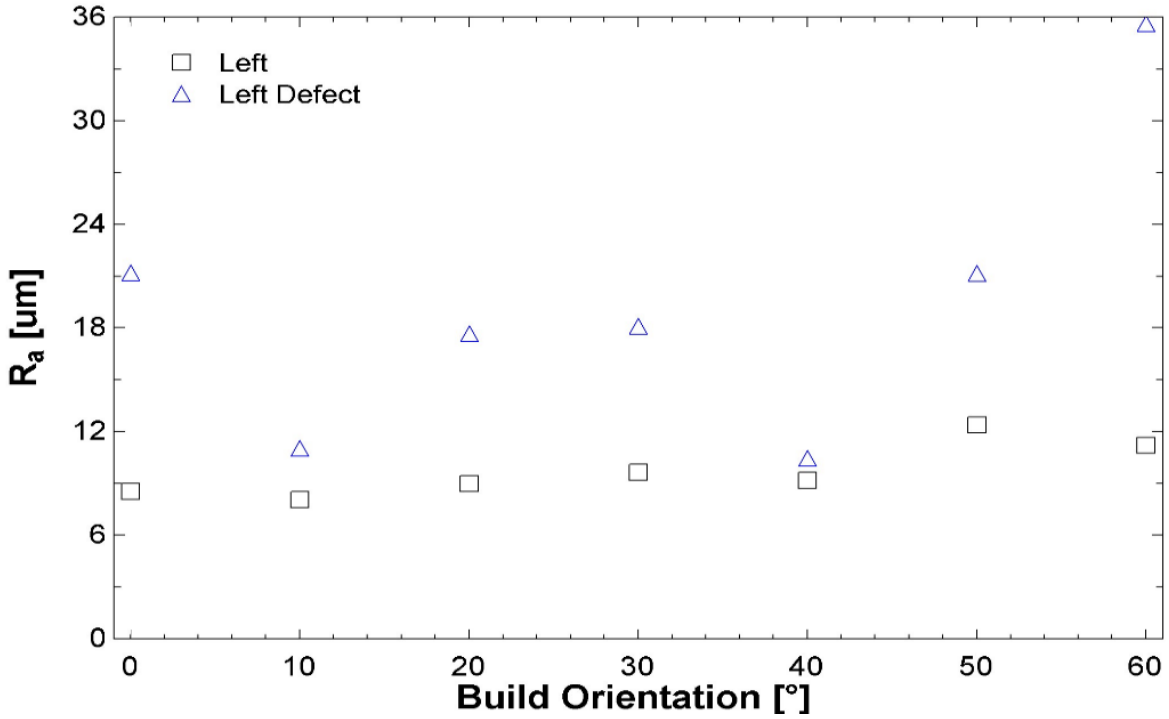

b)

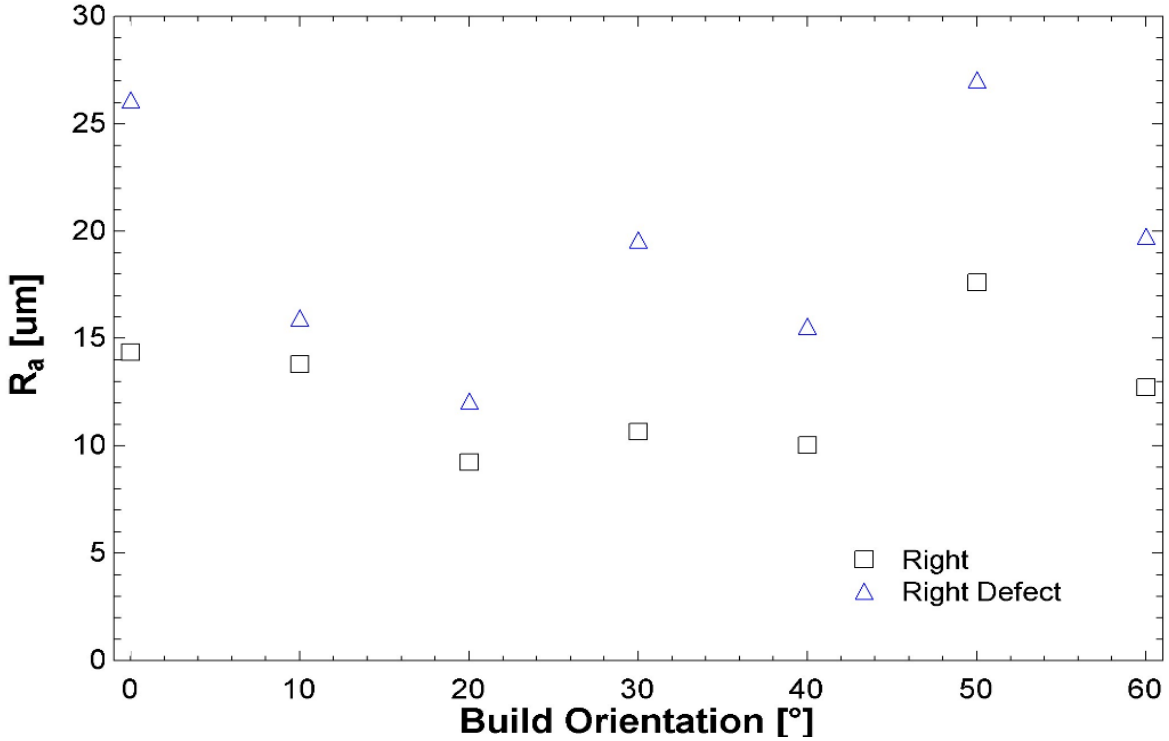

Figure 3.12: Average roughness for the a) left side of the pillar and a defect on the left side of the pillar b) right side of the pillar and a defect on the right side of the pillar for each build orientation. Adapted from [Figure 12]; Copyright ASME. Credit to Jordan Morrow for creating this graph [1].

3.4 Conclusions

Trends of water contact angles of water on AlSi10Mg surfaces manufactured via LPBF and printing angle were discussed in this study. Several qualitative and quantitative measurements have been provided. Although the powdered AlSi10Mg alloy is typically hydrophobic, wettability varied based on build angle: build angles of 0˚ and 60˚ exhibited primarily hydrophilic behavior, build angles of 10˚ and 20˚ demonstrated a mix of hydrophobic and hydrophilic behavior, and hydrophobic behavior was observed for 30˚, 40˚, and 50˚ build angles. The build/printing angle affects the roughness of the surface as well as the size and number of partially melted metal beads formed due to gravitational and powder-bed-capillary effects during the LPBF process. It was determined that the surfaces printed at 30˚ and 40˚ printing angles had the smoothest overall surfaces and, therefore, the highest solid-liquid contact angles (i.e., consistently hydrophobic). Surfaces were not homogenous and measured surface roughness, *Ra*, ranged from 5-36 μm, and arithmetic mean heights, *Sa*, ranged from 15.52-21.71 μm with variations based on location. The size of the partially melted metal beads decreased as the printing orientation angle increased. This information will be used in further experiments to determine the desired printing angle of VCs. Based on this study, the effects of the printing angle did not conclusively change the surface roughness of different shaped geometries due to strong anisotropy in roughness observed. Due to the nature of LPBF, as well as the process factors used to produce the specimens of this study, the surface of the specimens contained significant mini-structures which may prove valuable in the aid of heat transfer and bubble formation in VCs.

Chapter 4 - Design and Manufacture of AlSi10Mg Vapor Chamber

4.1 Specimen Design and Manufacture

The VC for this experiment was produced via Laser Powder Bed Fusion (LPBF) from casting aluminum (AlSi10Mg) powder. The VC was produced using the same material and production method as the pillar structures in chapter 3 of this study. This material was chosen for its excellent thermal properties and relatively low cost. The thermal conductivity of the material used is important to consider because a material with poor thermal properties will not be able to sufficiently transfer the excessive heat to the fluid on the inside of the vapor chamber. The thermal conductivity of the heat treated AlSi10Mg powder used for this project was advertised at 170 ± 5 W/m·˚C. Another study proved that this thermal conductivity was accurate in casted materials with slight variations based on the direction of measurements [41]. While this is not as thermally conductive as a copper powder, which is frequently observed to be twice as conductive at ~400 W/m·˚C, the price to print with the copper was 4x higher. For this reason, in this study it was determined that it was not necessary to produce the vapor chamber with copper.

The design of the VC was centered around a hollow 10 cm x 10 cm x 1 cm box with 2-3 mm walls. The external surfaces of the VC were intentionally kept symmetrical and simple. Extruding from the box are 5 cylindrical features which were used to aid in the depowdering and the charging of the VC. The inside of the VC was created with three geometric features designed to maximize the heat transfer to the working fluid, and therefore maximize the heat dissipation. An isometric view of this VC can be seen in Fig 4.1.

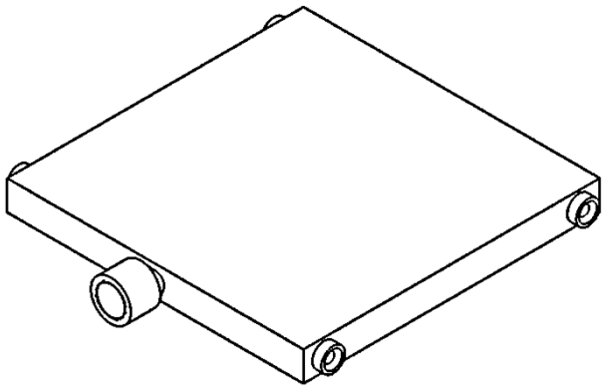

Figure 4.1: Isometric, external view of the manufactured vapor chamber.

Located on the front of the VC protrudes the charging port. This 13.5 mm diameter cylindrical feature was designed to contain 1/8" NPT threading (10.242 mm, 27 TPI) around its internal perimeter, designed to fit a high-torr vacuum fitting which would connect to the rest of the test setup. This fitting was intended to be sealed in place with thread locker to prevent air leaks once the charging process had begun. The threaded feature was not printed because it was determined that the AM process could not produce threading accurate enough to ensure the part could remain hermitically sealed. Connecting to the threaded feature was a 1.3 mm diameter pipe which was printed to connect the threaded opening to the interior of the vapor chamber. A drawing print of these features can be seen in Figure 4.2.

Located on the sides of the VC protrudes the evacuating ports. These 8 mm diameter cylindrical features were designed in much the same way as the charging port. The main difference is that these features were designed to be used in the depowdering process and then be permanently sealed off by using short M3 screws with thread locker. Similar to the charging port, the conical feature inside of the protruding cylinders was tapped and threaded via subtractive manufacturing rather than created additively to ensure the VC remained hermitically sealed. A drawing print of these features can be seen in Figure 4.3.

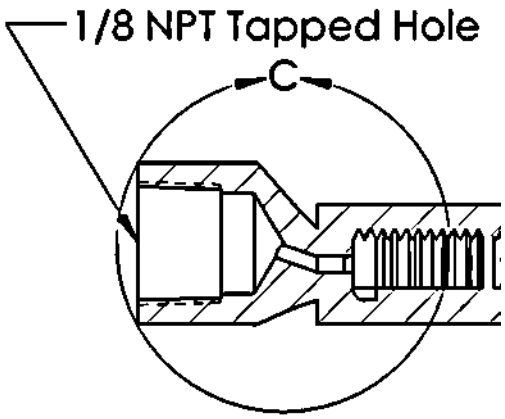

Figure 4.2: Side view of 1/8" NPT charging port.

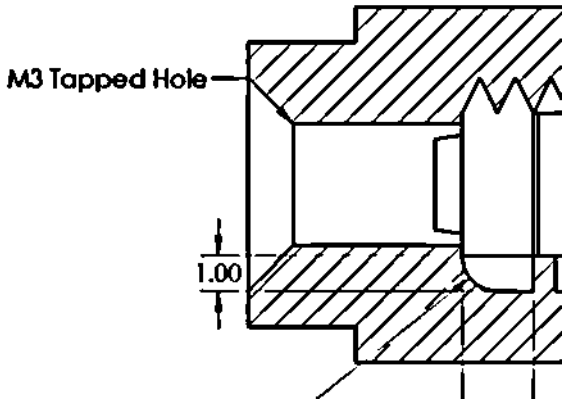

Figure 4.3: Side view of M3 evacuating port.

The bottom of the VC was created with a 26.5 mm square in the center of the part which was the same size of the high wattage heater. This square was added to maximize the heat transfer to the working fluid by minimizing the material between the heater and the working fluid. Centered around this square were 42 channels which provided a path for fluid flow from the center of the part to the walls of the VC. The number of channels was chosen to maximize the fluid flow by maximizing the wicking effect from the center of the VC to the outer walls. The walls of the VC contain a 2 mm wide, 1mm deep trench circumnavigating the rest of the features on the bottom of the VC. A drawing of these features can be seen in Figure 4.4.

Li et al. found that the wicking effect in a circular VC can be increased using a 1-mm wide inner channel with at least 1-mm distance between channels [42]. As the number of channels increased, the space between them decreased. The value that maximized the number of channels, while maintaining a space of at least 1 mm between them, was found to be 42. The outer width of the channel was calculated using [10]:

$$W_{\text{outer}} = W_{\text{inner}} \cdot m \tag{4}$$

where W_{outer} is the width of the outer wicking channel, W_{inner} is the width of the inner wicking channel (1mm) and:

$$m = \frac{2\pi R^2 \varphi}{nLW_{\text{inner}}} - 1 \tag{5}$$

where R is the length of wicking channels, which varies for each channel, φ is the volume fraction of high conductivity material (25% in this study), n is the total number of channels (42 in this study), and L is the distance from part center to the outside of the wicking channels, which varies for each channel.

The VC designed herein is based on those of Liu et al and Li et al. [10, 42]. In addition, the current study aims to determine how additive manufacturing and its generated materials influence VC operation and not necessarily how VC design impacts its performance. For the current VC design, the width of the channels was intentionally created to be larger as it approached the perimeter and to gradually decrease as it got closer to the center. This was done to promote vapor condensation closer to the evaporator. These channels existed only on the evaporator side of the VC.

The middle of the VC was designed to contain a large number of support structures which also functioned as wicking structures to pull condensing fluid from the cooler side (top) of the VC to the heated side (bottom) of the VC. These support/wicking structures were all located in the

spaces between the channels. Each wicking/support structure spanned the entire 6mm internal gap of the VC and had a 1 mm^2 cross-sectional area. A fill pattern was used such that the minimum distance between the center points of each pillar was 2 mm. To maximize the number of these pillars, the fill pattern had a 30˚ orientation from the binding edge, which was the edge nearest to the closest corner. On the internal sides of the VC, there were 1mm channels spaced 1mm apart in order to promote the movement of working fluid between the top and bottom of the VC. A drawing print of these features can be seen in Figure 4.5.

The top of the VC was designed to promote the condensation of the working fluid by providing geometries that increase surface area and promote capillary pressure; therefore, a mesh structure was created. The mesh structure was created by patterning a simple 1-mm tall pyramid with a 1-mm square base across the entire top surface of the VC. Pyramids were chosen because of their relatively simple geometry making it easy to pattern and because of their reduced volume compared to mesh structures of different geometries [43]. It is important to note that the pointed tips of the pyramid structures could not be produced perfectly sharp as a function of the LPBF process; therefore, the tips are rounded at the top. A drawing of these features can be seen in Figure 4.6.

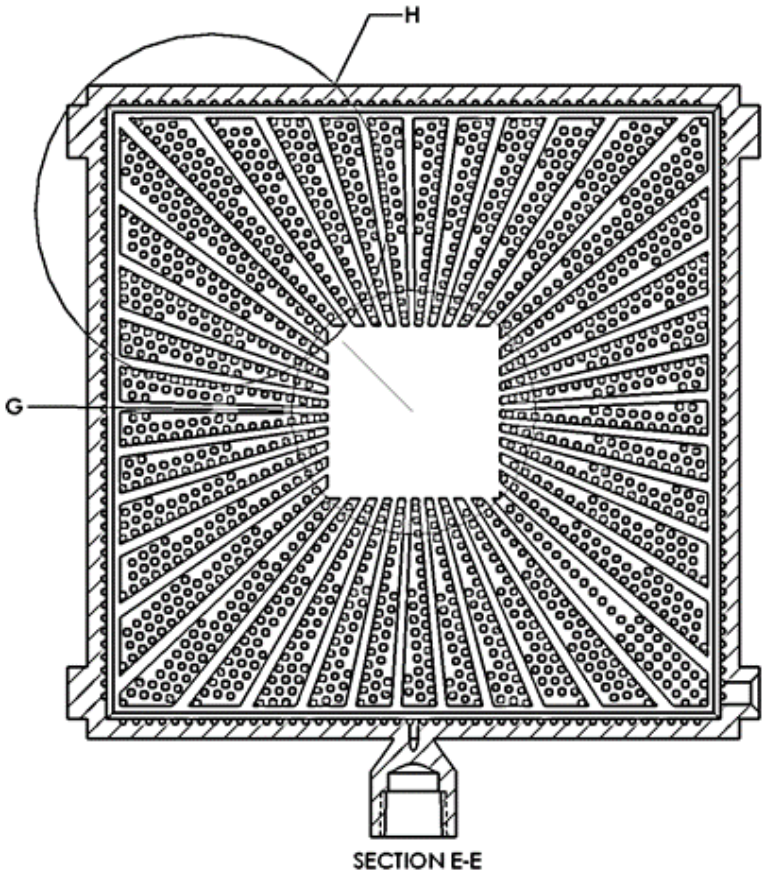

Figure 4.4: View of the bottom of the vapor chamber showing the features created by the addition of 42 circumferential channels and the surrounding trench.

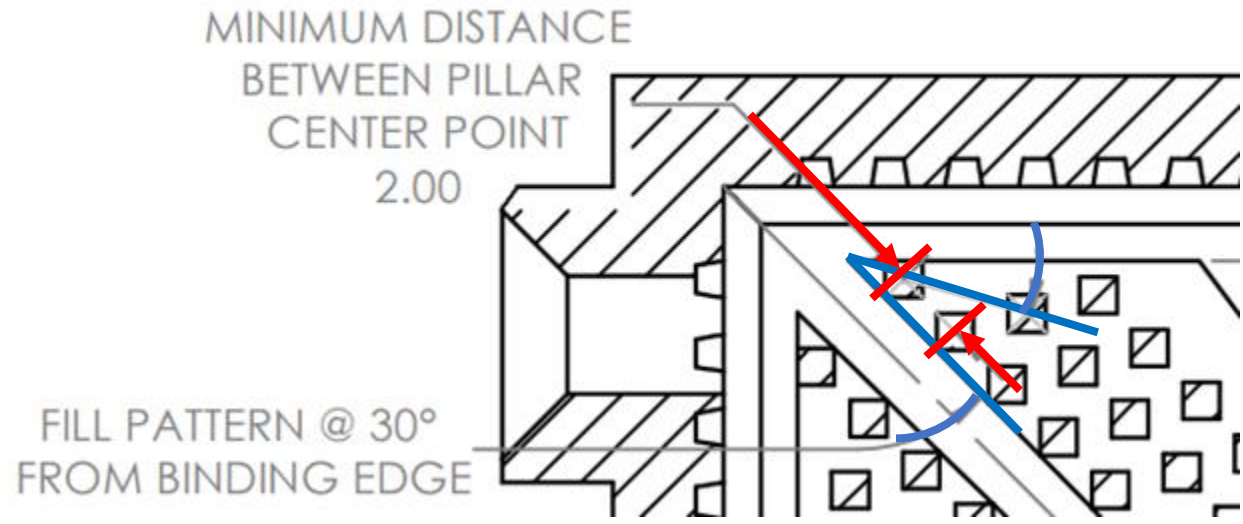

Figure 4.5: Close up view of the filling pattern used to create the support/wicking structures. The distance between the centers of the closest pillars was no less than 2 mm (shown in red). The angle between each row of pillars and the side of channel closest to the corner was 30˚ (shown in blue).

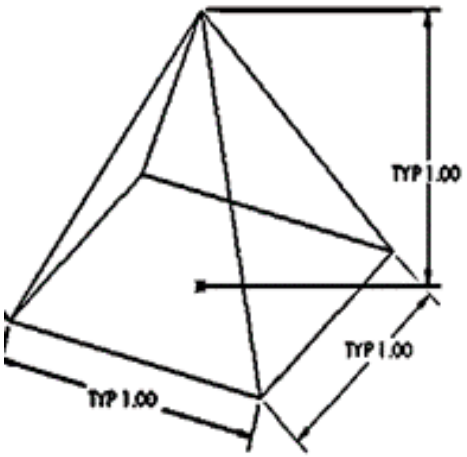

Figure 4.6: Close up view of the pyramidal geometry used in the meshing structure on the top of the vapor chamber.

The VC was printed at a 45˚ orientation from the normal surface of the part. This was done using previously determined data to maximize the fluid contact angles on the interior of the VC, meaning that this part was produced so that the metal surface would be hydrophobic [44]. The VC was produced to maximize hydrophobicity to increase the internal flow rate of the working fluid, thus increasing the heat transfer rate of the VC. Upon completion of printing, the vapor chamber was completely sealed, trapping the AlSi10Mg powder inside. The charging and evacuating ports were drilled and tapped to expose the inside of the VC. This is the only instance of subtractive manufacturing that was utilized in this study. Most of the powder easily removed by blowing compressed air into each of the ports. It was possible to temporarily close off individual ports by placing the M3 screws into the evacuating ports without thread locker in order to direct the flow of compressed air through different locations in the VC. Once it was no longer feasible to depowder the VC with compressed air, isopropyl alcohol (98+% purity) was injected into the charging port while temporarily closing the evacuating ports. The charging port was then also temporarily sealed, and the VC was placed in an ultrasonic shaker operating at room temperature

and 40kHz. This process was repeated several times until the VC was cleared of any remaining AlSi10Mg powder. The digital scale was used to determine whether the weight of the VC nearly matched the theoretical weight from a CAD software. Due to the size of the individual AlSi10Mg particles being too light to accurately determine complete depowdering, it was also necessary to rinse the inside of the VC until there were no AlSi10Mg particles present in the runoff and when the weight was no longer changing between cleanings.

A full drawing print of the vapor chamber can be found in Appendix A.

4.2 Experimental Methods

There were two steps involved in experimentally characterizing the VC. The first step required charging the VC to its ideal fill ratio. A study conducted by Wiriyasart and Naphon, who also used a wicking structure layer with solid columns, found that the optimum fill ratio to obtain minimum vapor chamber thermal resistance is about 32-34% by volume [44]. To quantify the thermal performance of the VC, effective thermal conductivity experiments were conducted when the VC was uncharged (control group) and when the VC was filled to approximately 30% capacity with degassed-deionized water. To make it simpler to compare and interpolate the results of different filling ratios, the filling ratio chosen to be the "optimum" ratio was 30%. It was determined that the best way to determine whether the VC design was functioning as intended was to compare the thermal conductivity of the empty VC to the thermal conductivity of the VC with an optimal fill ratio. This comparison is helpful as a proof of concept for the VC design in order to justify obtaining additional data for other filling ratios for future research. This direct comparison is also a means to determine if the VC is operational and functioning as intended.

The correct filling ratio was obtained by filling the VC while it was on an scale and observing the change in weight as water was pulled into VC. The theoretical total internal volume of the VC was determined using Solidworks® to be 38.8 mL. This volume, affected by previously discussed partially melted metal beads, was verified to be accurate by weighing the empty part and comparing it to the theoretical part weight. Because the density of water is ~1 g/mL, a 30% filling ratio would result in adding 11.6 g of water. The VC was filled with 11.6 ± 1 mL of degassed-deionized water resulting in a filling ratio of 27.5 – 32.5%.

To fill the VC, a 500 mL beaker was partially filled with deionized water, connected to a cold trap and a Fisherbrand Maxima Rotary Vane vacuum pump (max vacuum 10^{-4} torr),

hermitically sealed, and placed inside of a heated ultrasonic shaker bath. The bath was turned on until the temperature reached ~40˚C to maximize boiling potential. Once the beaker reached a high enough temperature, the cold trap was filled with liquid nitrogen and the vacuum pump was turned on. The reduction in pressure inside of the beaker lowered the deionized water's boiling point. The+ deionized water almost immediately began to boil off excess O_2 which was pulled out of the beaker by the vacuum pump. This process continued until the system, measured by a pressure gage near the vacuum pump, reached a pressure of 10^{-3} torr and when the water had stopped boiling. This process can be visualized in Fig 4.7.

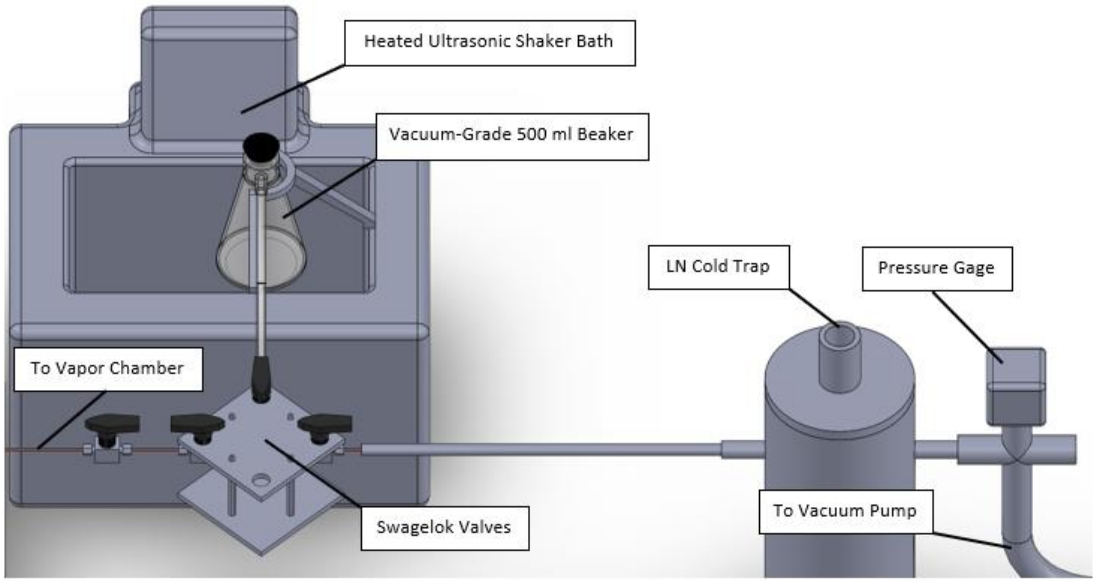

Figure 4.7 Vapor Chamber Charging Setup

Once the water had been degassed, the VC needed to be evacuated of air, as well. The Swagelok valve connecting the beaker to the vacuum pump was closed while the valve connected to the VC was opened which brought it to a pressure of at least 10^{-3} torr. In order to introduce the degassed water into the VC, there needed to be a pressure differential between the beaker and the VC. The pressure was subsequently increased in the beaker without allowing it to return to ambient pressure, between 10^{-1} and 10^{-2} torr. The valve connecting the vacuum pump was closed

and the valve connecting the VC to the system was slowly opened. The difference in pressure was enough that when the beaker was tipped over to allow water to flow into the system, it was pulled into the VC. The water was pulled into the VC until the desired fluid weight had been reached. A secondary Swagelok valve was set in place parallel to the charging port of the VC so that the forces applied to the rest of the system did not affect the weight applied to the high-resolution scale. Upon reaching the desired fluid weight, the charged VC was then removed from the charging system and hermitically sealed and cut by using a hydraulic crimper to close off the 1/16" copper charging tube between the secondary Swagelok valve and the charging port of the VC. This process is shown Fig 4.8.

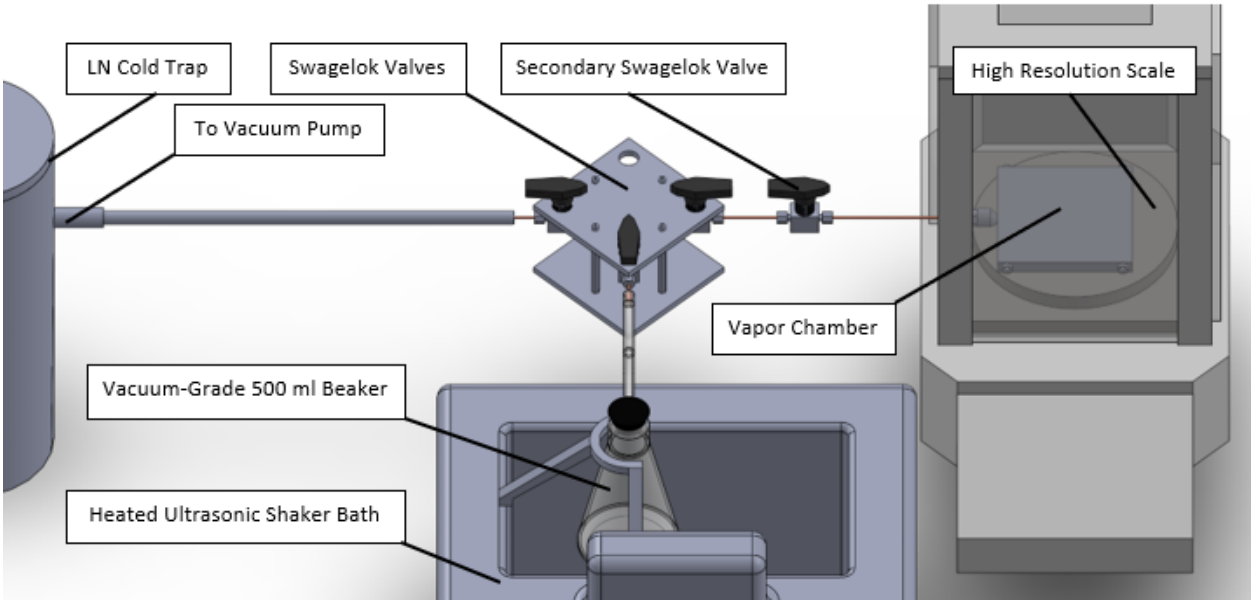

Figure 4.8 Vapor Chamber Charging Setup

The second step of the experimentation process began by taking the charged VC to the insulated experiment station. The thermally significant surfaces of the VC within the experimental setup were coated with Omegatherm 201 high thermal conductivity paste. The VC, along with a 3/16" copper thermocouple-holding plate, were clamped between the heater assembly and a water-cooling block inside of the experiment station.

After the experimental setup was bolted together by hand tightening, the bottom edge of the VC was leveled inside of the test stand and everything was insulated using fiberglass insulation to minimize ambient temperatures effecting the experiment. The cooling block was connected to the Polyscience LM61GX1A110C chiller and a Picomag BA01697D/06 flowmeter which controlled water flow rate and temperature flowing through the cooling block. An external view of this setup can be seen in Figure 4.9.

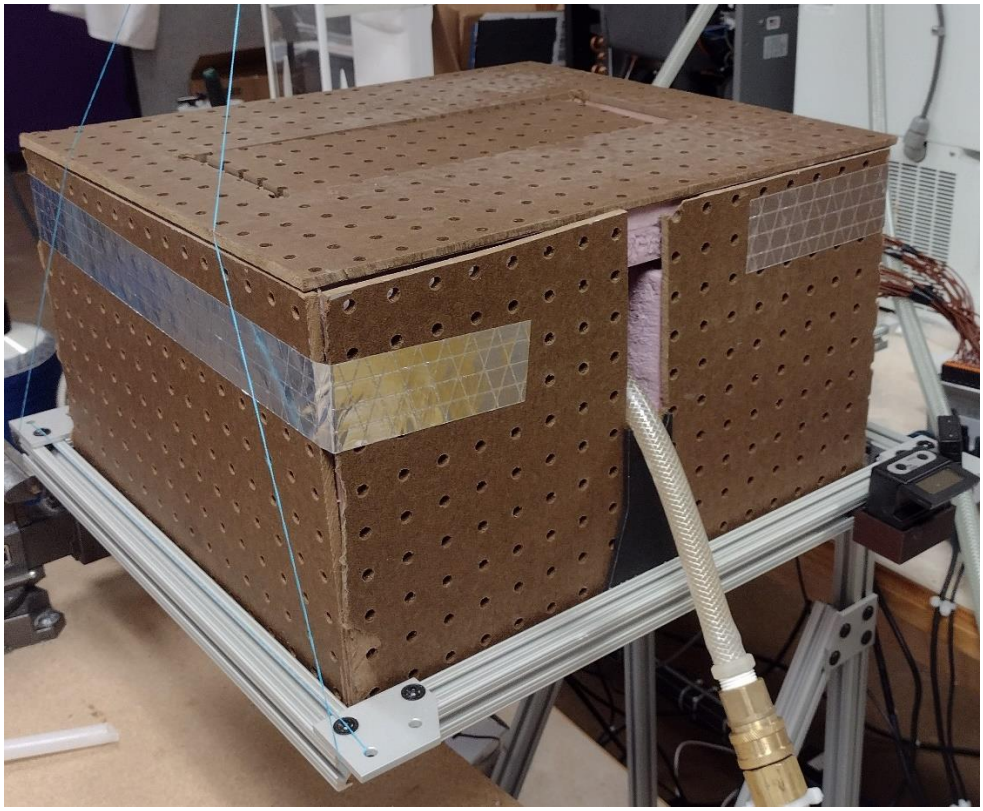

Figure 4.9: Fully insulated experiment with vapor chamber pre-installed.

Once the fiberglass insulation had been applied to the experimental setup, the Polyscience chiller was turned on and adjusted to 20 ± 0.5°C and the volumetric flow rate was adjusted by opening/partially closing one of the valves connected to the flow meter. The temperature was chosen because the chiller had a difficult time maintaining a lower starting temperature at the required volumetric flow rate. There were two volumetric flow rates used in this study, 4.9 ± 0.3

l/min which was the maximum flow rate possible and 2.4 ± 0.3 l/min which was used to determine whether the volumetric flow rate of the system had influence over the results of the experiment. Prior to turning on the heater, the chiller was allowed to run under these conditions until the thermocouples in the experiment reached steady state.

Upon achieving steady-state temperatures, the pre-experiment ambient temperatures were recorded, and the National Instruments software was turned on which recorded each thermocouple temperature at 50Hz continuously. The VI map block diagram and front panel are available in Appendix B. The variable power supply, which was used to apply a heat to the study, was then turned on to the required power for the experiment. Seven different power levels at 50W increments were experimented with: 350W, 300W, 250W, 200W, 150W, 100W, and 50W. Higher power levels up to 480W were possible; however, it was determined that higher wattages could result in dangerously hot temperatures inside of the insulated experiment. Once the power had been turned on to the appropriate level, the experiment was allowed to run undisturbed until the 13 thermocouples had reached steady state. Depending on the power level, this process could take as long as an hour. Once steady state had been achieved throughout the experimental setup, the software and the power supply were switched off while the chiller remained on at the same volumetric flow rate. This process was repeated once the thermocouples had returned to steady state temperatures. This process was repeated both charged and uncharged, at full cooling capacity and at half capacity, and at seven different heater wattages, for a total of 28 experiments. The data were logged onto an excel spreadsheet.

4.3 Results and Discussion

The experiments were conducted on the VC both empty and charged at a 30% filling ratio. The two sets of data were compared to determine whether the design of the VC was effective in dissipating concentrated thermal energy. The initial and final heater-side and condenser-side temperatures as well as the change in temperature were observed in each group of thermocouples. The groups were labeled as:

1. Heater temperature and absolute max temperature: Thermocouple 1.
2. Condenser-side group: Thermocouples 2-9.
3. Heater-side group: Thermocouples 10-13.

The resulting data all resulted in similar curves to what are shown in Figure 4.10.

a) *Heater*

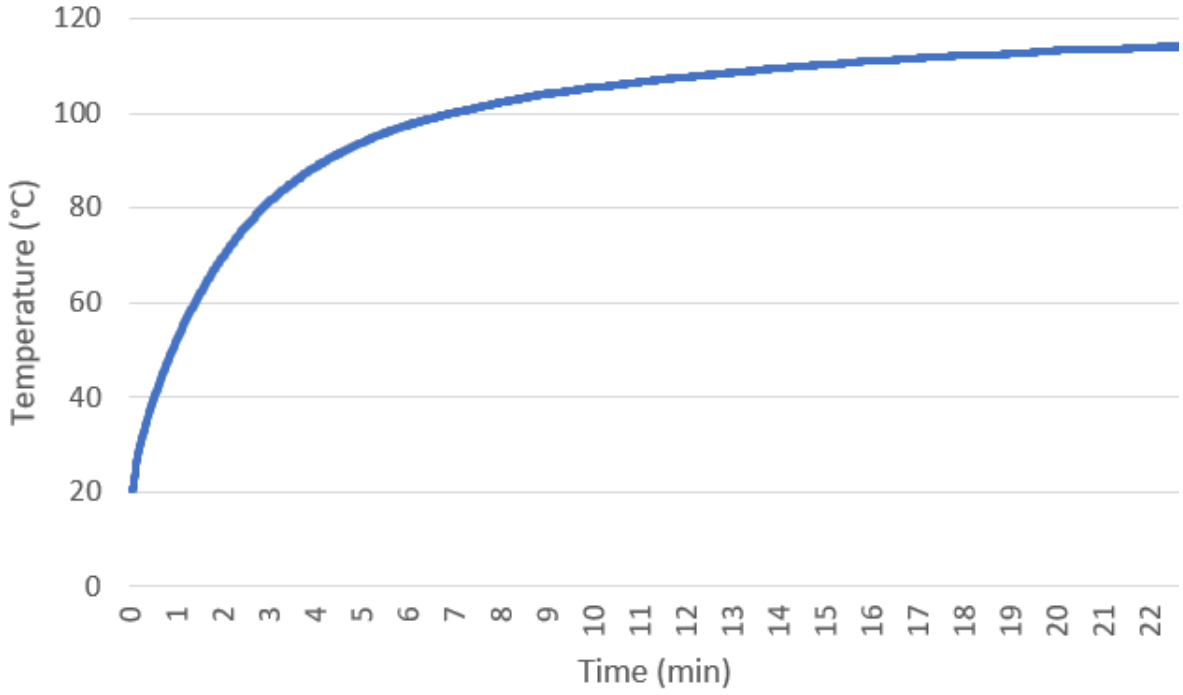

b) *Condenser-side thermocouples*

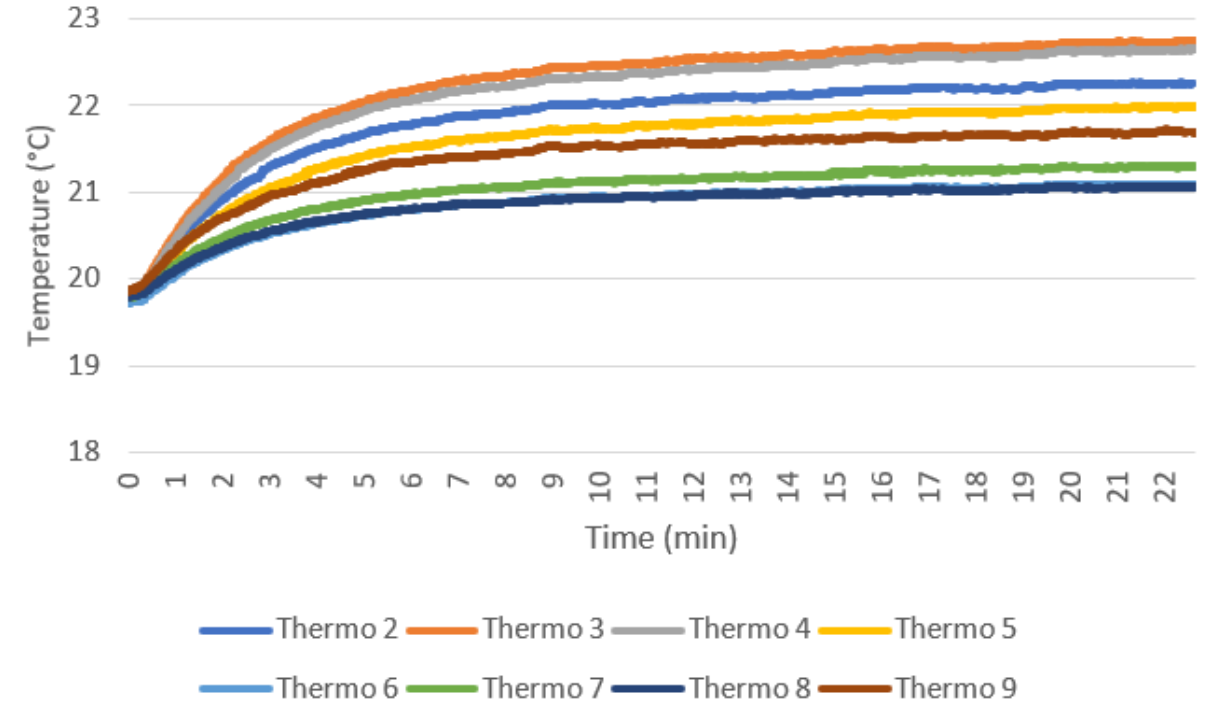

c) *Heater-side thermocouples*

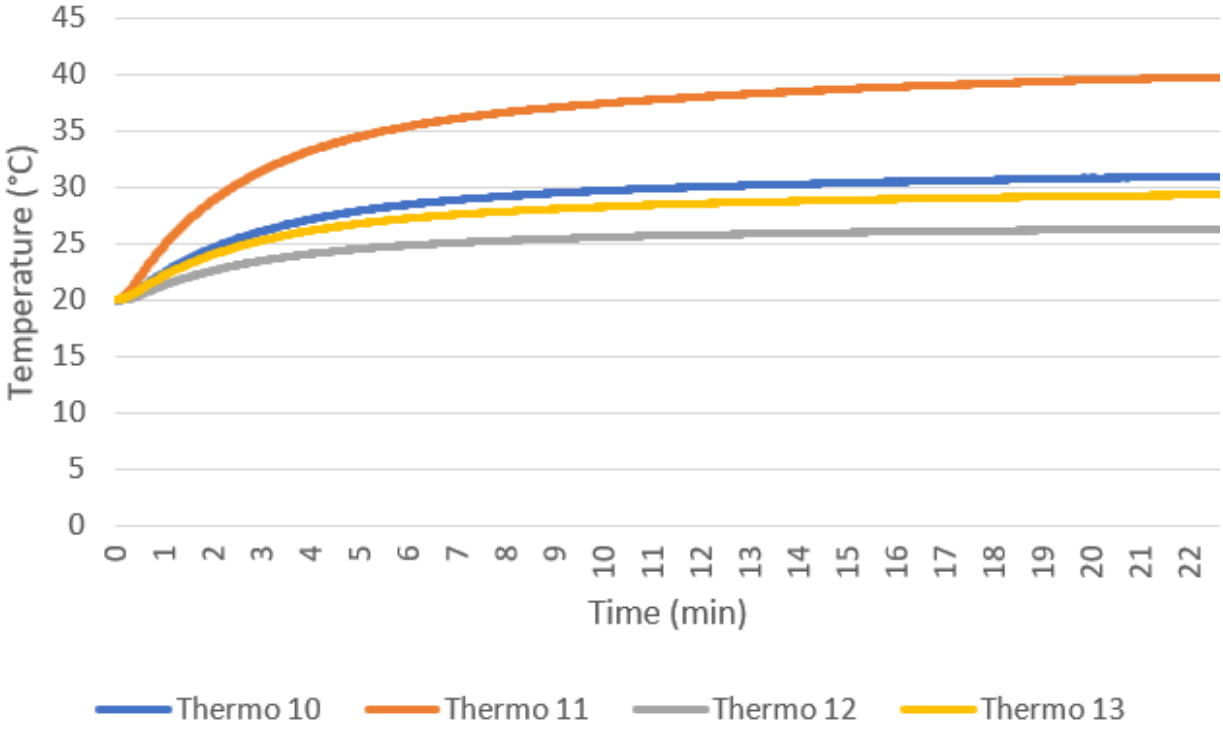

Figure 4.10: Experimental results for a 300W experiment. The x-axis is the time in minutes while the y-axis is the temperature in degrees C.

Thermocouples 2-9 were observed to try to obtain a temperature profile across the condenser side of the VC. From the locations in Figure 2.3, thermocouples 5 and 6 should hypothetically have the highest temperature because they are closest to the location of the heater while thermocouples 2 and 9 should hypothetically have the lowest temperature being farthest from the heater. It was observed that the temperatures across the condenser side of the VC did not consistently show this trend. Thermocouples 5 and 6 were the closest to the center of the VC but did not always show the highest readings. The average temperature across the condenser-side of the VC was instead used to obtain datapoints in further calculations. The average condenser side temperature was compared to the average value of the four heater side thermocouples as well as the heater temperature.

After all 28 experiments were run, the data were compiled to average the last 120 seconds of temperature readings for all thermocouples. These final two minutes of datapoints were used to obtain the average steady-state condenser-side, heater-side, and heater temperatures for the experiment with. The average condenser-side temperatures were compared to the average heater-side temperatures at steady-state to plot a ΔT vs Q curve in excel. The resulting data can be seen in Tables 2 and 3 as well as Fig 4.11. The difference between the charged VC and the empty VC was calculated and shown in tables 2 and 3 as "% Change". In all experiments, the T and ΔT were greater in the charged VC than in the empty VC.

Table 2: Average steady-state temperatures for the vapor chamber at various power inputs. The percent change value is the average difference between the charged and empty experiments. All temperature values are in units of °C.

a) *Condenser-side final temperatures*

Power (W)	Charged		Empty		% Change
	2.4-2.5 l/min	4.8-4.9 l/min	2.4-2.5 l/min	4.8-4.9 l/min	
350	22.86	22.51	22.75	22.20	0.93
300	22.09	21.84	21.92	21.75	0.61
250	21.38	21.23	21.25	21.12	0.56
200	20.85	20.72	20.65	20.55	0.89
150	20.31	20.28	20.19	20.07	0.84
100	20.04	20.07	19.78	19.77	1.41
50	19.87	19.85	19.58	19.58	1.43

b) *Heater-side final temperatures*

Power (W)	Charged		Empty		% Change
	2.4-2.5 l/min	4.8-4.9 l/min	2.4-2.5 l/min	4.8-4.9 l/min	
350	36.22	35.44	34.70	34.72	3.16
300	31.88	31.59	30.60	30.40	3.96
250	27.92	27.73	27.38	27.22	1.91
200	25.12	24.83	24.63	24.41	1.86
150	22.54	22.53	22.29	22.15	1.42
100	21.11	21.23	20.87	20.75	1.71
50	20.24	20.27	19.92	19.89	1.75

Table 3: Difference in temperature between the condenser and heater-side thermocouples at various power inputs. The percent change value is the average difference between the charged and empty experiments. All values are in units of °C.

Power (W)	Charged		Empty		% Change
	2.4-2.5 l/min	4.8-4.9 l/min	2.4-2.5 l/min	4.8-4.9 l/min	
350	13.36	12.93	11.96	12.52	6.43
300	9.78	9.74	8.68	8.65	6.79
250	6.54	6.50	6.13	6.10	6.81
200	4.27	4.11	3.98	3.86	7.12
150	2.23	2.25	2.10	2.08	7.19
100	1.08	1.15	1.10	0.98	11.91
50	0.37	0.42	0.34	0.31	19.28

a) *Condenser-side thermocouples*

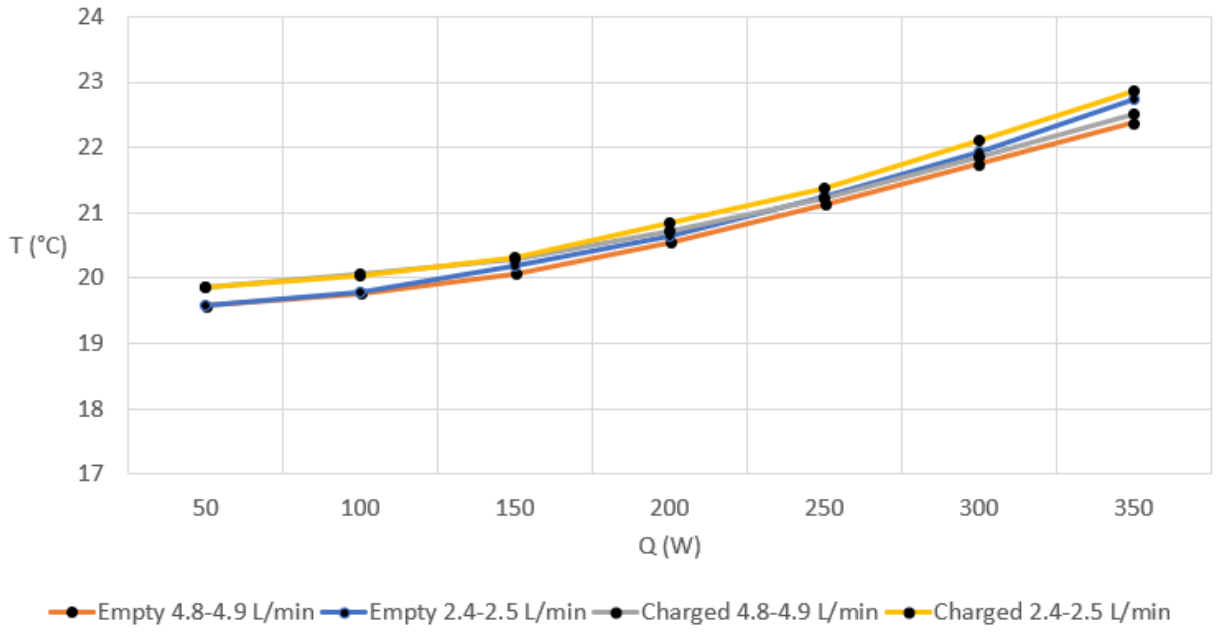

b) *Heater-side thermocouples*

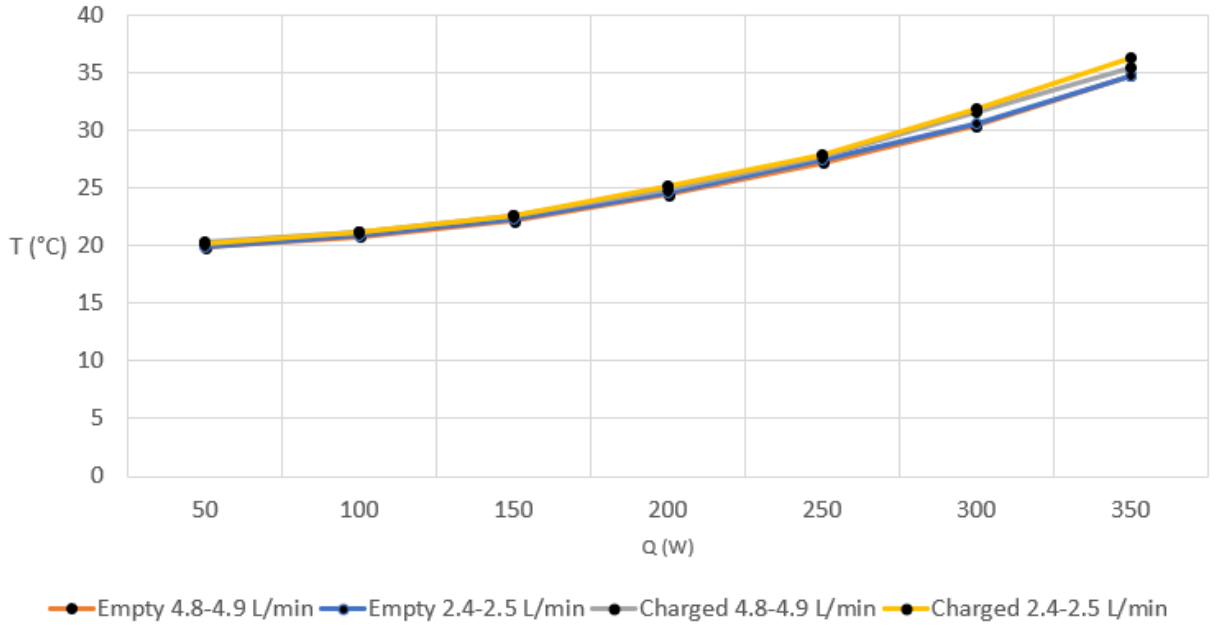

c) *ΔT vs Q*

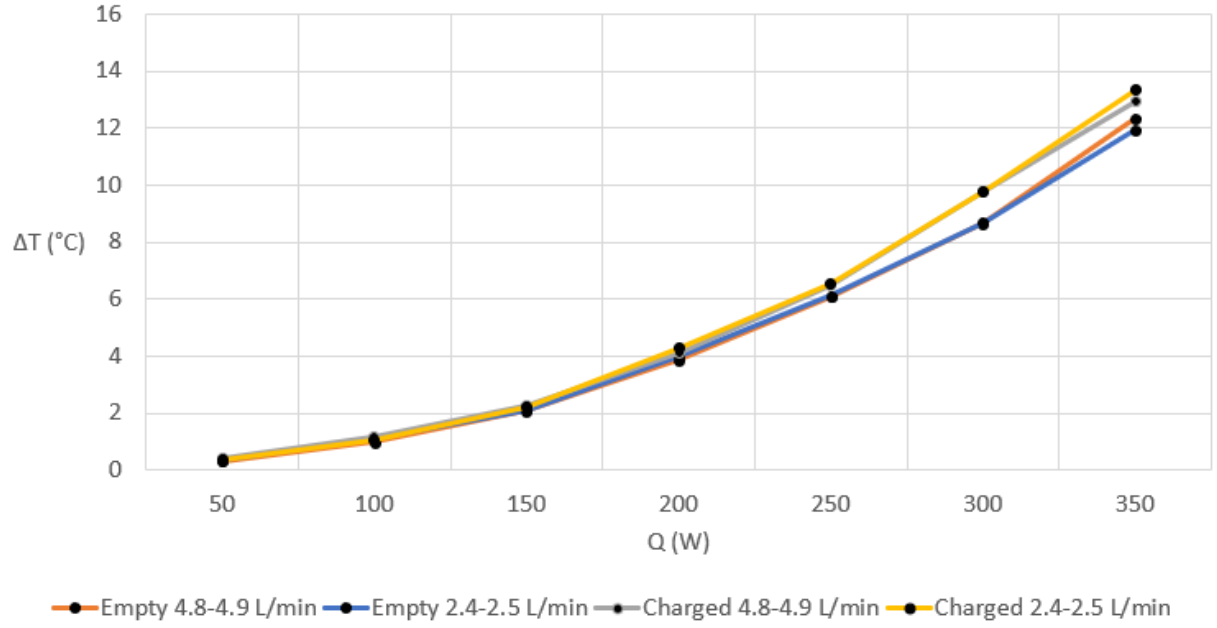

Figure 4.11: a) Average steady-state condenser side temperature. b) Average steady-state heater side temperature. c) Change in temperature during transient temperature state.

What can be deduced from these results is that while the absolute temperatures between the charged and uncharged VC are very similar, the overall temperature difference across the system increases. This implies that the experiment did not yield results proving the effectiveness of the VC's design. If the experiments were to yield successful results, the temperature difference across the charged VC would be lower than with the empty VC.

The apparent failure of this experiment may be explained in one of two ways. The first explanation is that the VC did not remain hermitically sealed once it had been charged. This is a distinct possibility considering the necessity to hermitically seal five different ports. If any one of those ports were to be improperly sealed, it would not hold a vacuum and the VC would not yield conclusive results. This hypothesis was tested by dunking the sealed VC in a tank of water and cutting the 1/16" copper tube to release any air/vacuum inside of the VC. If the vacuum had indeed

been released, the VC would be expected to release air bubbles from the new opening in the copper tube or around one of the charging/evacuating ports; however, no such air bubbles ever formed.

The second explanation involved the thermal conditions of the experiment. The VC only reached the conditions necessary to start the multi-phase slug movement for one of the experiments. It's possible that either the surface of the heater didn't reach a high enough temperature or that the cooling block was too efficient to allow to allow the VC to reach the critical point necessary for successful multi-phase heat transfer. The results shown in Figure 4.12 from a 350W experiment provide a proof of concept for the VC's design; however, more experimentation at different thermal conditions is likely necessary to provide an efficiency. The sudden "dip" in all of the thermocouple readings is the beginning of phase-change heat transfer throughout the VC. The final steady-state temperatures are lower than they would otherwise be because of reaching this critical point.

a) *Heater*

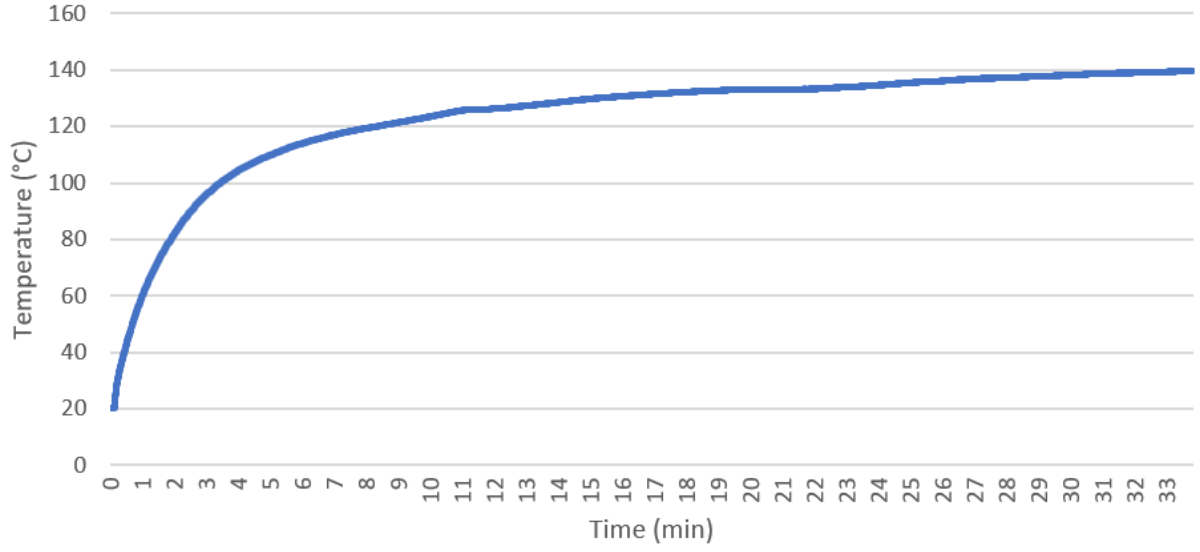

b) *Condenser-side thermocouples*

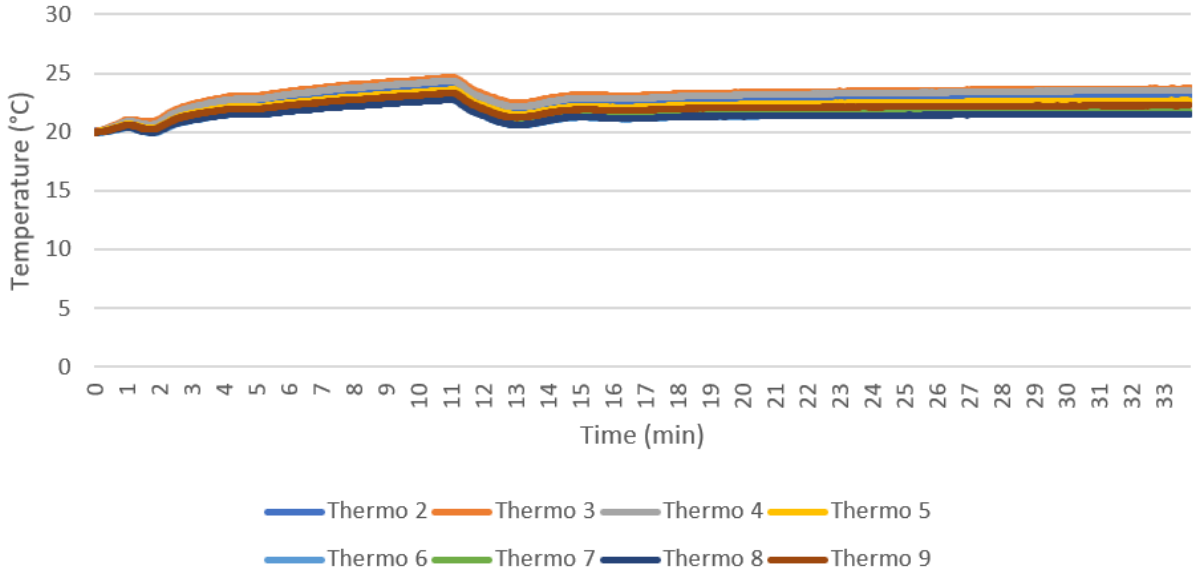

c) *Heater-side thermocouples*

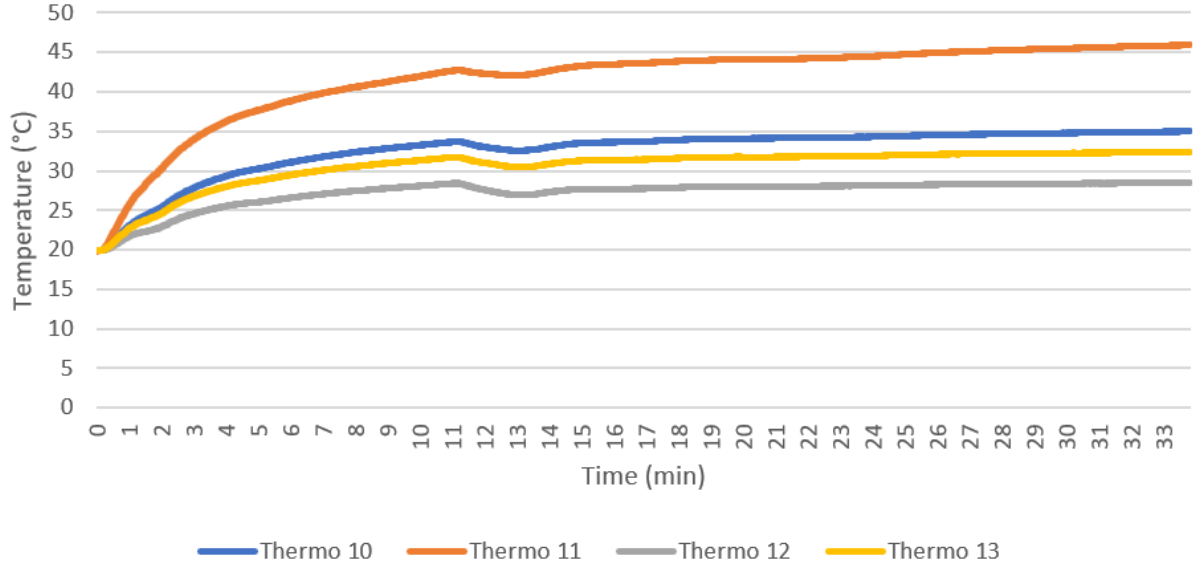

Figure 4.12: Experimental results for a charged 350W experiment. The x-axis is the time in minutes while the y-axis is the temperature in degrees C.

4.4 Conclusions

The manufacturing of an AlSi10Mg vapor chamber has been successful; however, based on the results obtained at this point in the study, the effectiveness of the design of the vapor chamber could not be determined. Through the manufacturing process of this study, it was found that high resolution geometries could be produced within an entirely enclosed feature. This study also found that the depowdering process required to remove the excess internal production material was successfully implemented to fully empty the vapor chamber of aluminum powder. The charging process required to create a fully functional vapor chamber was also successfully implemented and provided a proof of concept for additively manufacturing multi-phase heat spreaders.

Additional experiments under different heating and cooling conditions may have to be conducted in the future before this study will yield conclusive thermal conductivity results. It is believed that the VC would perform better at higher filling ratios. Once more favorable results are obtained, thermal resistances can be calculated from the thermocouple values as well as some of the heating and cooling conditions such as the heater temperature and the water temperature inside of the cooling system. Once the thermal resistances are calculated, a thermal conductivity of the vapor chamber can be obtained and compared to different filling ratios. Further studies in this field may consider the exploration of different internal geometrical designs to directly compare the effectiveness of a vapor chamber produced via laser powder bed fusion to a traditionally manufactured vapor chamber.

References

[1] Christopher M. Bailey, Jordan A. Morrow, Emily M. Stallbaumer-Cyr, Cameron Weeks, Melanie M. Derby, Scott M. Thompson, "Effects of Build Angle on Additively Manufactured Aluminum Alloy Surface Roughness and Wettability", *ASME Journal of Manufacturing Science and Engineering*, Vol 144, 2022.

[2] MA, H., 2016, Oscillating Heat Pipes. Springer Science + Business Media New York 2015, pp. 389.

[3] Davoud Jafari, Wessel W. Wits, Bernard J. Geurts, Phase change heat transfer characteristics of an additively manufactured wick for heat pipe applications, *Applied Thermal Engineering*, Vol. 168, 2020, 114890.

[4] Thompson, Scott & Ma, Hongbin. Recent Advances in Two-Phase Thermal Ground Planes. *Annual Review of Heat Transfer*, 2015, 2015011163.

[5] Zhao, C., Fezzaa, K., Cunningham, R.W. et al. Real-time monitoring of laser powder bed fusion process using high-speed X-ray imaging and diffraction. *Sci Rep 7, 3602,* 2017.

[6] Bailey, Christopher M. Weeks, Cameron. Thompson, Scott M. "Design and Performance of a Novel AlSi10Mg Vapor Chamber Fabricated via Laser Powder Bed Fusion" Solid Freeform Fabrication Conference. Paper 63599: Virtual Event, August 2-4, 2021.

[7] ASTM Standard 52900:E, 2015, "Standard Terminology for Additive Manufacturing -General Principles- Terminology," ASTM International, West Conshohocken, PA, 2016.

[8] Gennaro Salvatore Ponticelli, Oliviero Giannini, Stefano Guarino, Matthias Horn, An optimal fuzzy decision-making approach for laser powder bed fusion of AlSi10Mg alloy, *Journal of Manufacturing Processes*, Vol. 58, 2020, pp. 712-723.

[9] A. du Plessis, S. Beretta, Killer notches: The effect of as-built surface roughness on fatigue failure in AlSi10Mg produced by laser powder bed fusion, *Additive Manufacturing*, Vol. 35, 2020, 101424.

[10] Wangyu Liu, Yi Peng, Tao Luo, Yuanqiang Luo, Kaidong Huang, The performance of the vapor chamber based on the plant leaf, *International Journal of Heat and Mass Transfer*, Vol. 98, 2016, pp. 746-757.

[11] Esarte, J., Blanco, J., Bernardini, A., & San-José, J. (2017). Optimizing the design of a two-phase cooling system loop heat pipe: Wick manufacturing with the 3D selective laser melting printing technique and prototype testing. *Applied Thermal Engineering*, Vol. 111, 2016, pp. 407-419.

[12] Jafari, D., Wits, W. W., & Geurts, B. J. (2017). An investigation of porous structure characteristics of heat pipes made by additive manufacturing. Paper presented at the 2017 23rd International Workshop on Thermal Investigations of ICs and Systems (THERMINIC).

[13] Jafari, D., Wits, W. W., & Geurts, B. J. (2018). Metal 3D-printed wick structures for heat pipe application: Capillary performance analysis. *Applied Thermal Engineering*, Vol. 143, 2018, pp. 403-414.

[14] Hadley Brooks, Kevin Brigden, Design of conformal cooling layers with self-supporting lattices for additively manufactured tooling, *Additive Manufacturing*, Vol. 11, 2016, pp. 16-22.

[15] Scott M. Thompson, Zachary S. Aspin, Nima Shamsaei, Alaa Elwany, Linkan Bian, Additive manufacturing of heat exchangers: A case study on a multi-layered Ti–6Al–4V oscillating heat pipe, *Additive Manufacturing*, Vol. 8, 2015, pp. 163-174.

[16] DU, Y., & TONG, P. Turbulent thermal convection in a cell with ordered rough boundaries, *Journal of Fluid Mechanics*, Vol. 407, 2000, pp. 57-84.

[17] S. M. Demsky & H. B. Ma . “Thin film evaporation on a curved surface.”, *Microscale Thermophysical Engineering*, pp. 285-299, 2004.

[18] Chi Young Lee, Wang Kee In. Prediction of water droplet evaporation on zircaloy surface, *Journal of Nuclear Science and Technology*, Vol. 51:4, 2014, pp. 448-456.

[19] Fathi, Parisa & Mohammadi, Mahyar & Nasiri, A. Low Surface Roughness Additively Manufactured AlSi10Mg: *The Impacts on Corrosion and Water Repellency Properties*. 2020, pp. 209-320.

[20] Koishi Takahiro, Yasuoka Kenji, Fujikawa Shigenori, Ebisuzaki Toshikazu, Zeng Xiao Cheng, “Coexistence and transition between Cassie and Wenzel state on pillared hydrophobic surface.” *Proceedings of the National Academy of Sciences*, Vol. 106 (21), 2009.

[21] Combined Visualization and Heat Transfer Measurements for Steam Flow Condensation in Hydrophilic and Hydrophobic Mini-Gaps, *Journal of Heat Transfer*, Vol. 138, 2016.

[22] A review of dropwise condensation: Theory, modeling, experiments, and applications." *International Journal of Heat and Mass Transfer* Vol. 160, 2020, 120172

[23] Attinger, D., Frankiewicz, C., Betz, A., Schutzius, T., Ganguly, R., Das, A., Chang-Jin, K., Megaridis, C. Surface engineering for phase change heat transfer: A review. *MRS Energy & Sustainability*, Vol. 1, 2014.

[24] Leis A, Weber R, Graf T. Process Window for Highly Efficient Laser-Based Powder Bed Fusion of AlSi10Mg with Reduced Pore Formation. *Materials (Basel)*, Vol 14, 2021.

[25] Li, Baoqiang & Li, Zhonghua & Bai, Peikang & Liu, Bin & Kuai, Zezhou. Research on Surface Roughness of AlSi10Mg Parts Fabricated by Laser Powder Bed Fusion. *Metals*, Vol 8, 2018.

[26] Mohammad Montazeri & Prahalada Rao. Sensor-Based Build Condition Monitoring in Laser Powder Bed Fusion Additive Manufacturing Process Using a Spectral Graph Theoretic Approach, *Journal of Manufacturing Science and Engineering*, Vol. 140, 2018.

[27] Slegers, Sam & Linzas, Mathias & Drijkoningen, Jeroen & D'Haen, Jan & Reddy, Naveen & Deferme, Wim. Surface Roughness Reduction of Additive Manufactured Products by Applying a Functional Coating Using Ultrasonic Spray Coating. *Coatings*. Vol. 7, 2017.

[28] Tao Yang, Tingting Liu, Wenhe Liao, Eric MacDonald, Huiliang Wei, Xiangyuan Chen, Liyi Jiang, The influence of process parameters on vertical surface roughness of the AlSi10Mg parts fabricated by selective laser melting, *Journal of Materials Processing Technology*, Vol. 266, 2019, pp. 26-36.

[29] Wenhui Yu, Swee Leong Sing, Chee Kai Chua, Xuelei Tian, Influence of re-melting on surface roughness and porosity of AlSi10Mg parts fabricated by selective laser melting, *Journal of Alloys and Compounds*, Vol. 792, 2019, pp. 574-581.

[30] Kuisat, Florian et al. Simultaneous Micro-Structuring and Surface Smoothing of Additive Manufactured Parts Using DLIP Technique and Its Influence on the Wetting Behaviour. *Materials (Basel, Switzerland)*, Vol. 14(10), 2021.

[31] Ali Davoudinejad, Yukui Cai, David Bue Pedersen, Xichun Luo, Guido Tosello, Fabrication of micro-structured surfaces by additive manufacturing, with simulation of dynamic contact angle, *Materials & Design*, Vol. 176, 2019.

[32] Snyder, J. C., and Thole, K. A. (May 6, 2020). "Understanding laser powder bed fusion surface roughness." ASME. *J. Manuf. Sci. Eng*. Vol.142(7), 2020.

[33] Anna Luise Strauch, Volker Uhlenwinkel, Matthias Steinbacher, Felix Großwendt, Arne Röttger, Abootorab Baqerzadeh Chehreh, Frank Walther and Rainer Fechte-Heinen, Comparison of the Processability and Influence on the Microstructure of Different Starting Powder Blends for Laser Powder Bed Fusions of a Fe3.5Si1.5C Alloy. *Metals 2021*. Vol 11(7), 2021.

[34] P.Wang, L Deng, K.G. Prashanth, S.Pauly, J.Eckert, S.Scudino. Microstructure and mechanical properties of Al-Cu alloys fabricated by selective laser melting of powder mixtures. *Journal of Alloys and Compounds*. Vol 735, 2018.

[35] E.O. Olakanmi, R.F. Cochrane, K.W. Dalgarno, A review on selective laser sintering/melting (SLS/SLM) of aluminium alloy powders: Processing, microstructure, and properties, *Progress in Materials Science*, Vol. 74, 2015, pp, 401-477.

[36] Yu-Hsun Hung, Shung-Wen Kang, and Wan-Chun Tsai. "Strain analysis of vapor chamber heat spreaders." *Journal of Marine Science and Technology*. Vol 18, No. 2, pp. 277-283, 2010.

[37] Lin-zhi Wang, Sen Wang, Jiao-jiao Wu, Experimental investigation on densification behavior and surface roughness of AlSi10Mg powders produced by selective laser melting, *Optics & Laser Tech.*, Vol. 96, 2017, pp. 88-96.

[38] Carey, V. P. *Liquid-vapor phase-change phenomena 2nd edition*. Hemisphere. 2008, pp. 55.

[39] J M Dubois *et al*. Measurements of contact angles of water on Al-based intermetallic surfaces, *Journal of Physics: Condensed Matter*, Vol. 20, 2008.

[40] Alberto Boschetto, Luana Bottini, Francesco Veniali, Roughness modeling of AlSi10Mg parts fabricated by selective laser melting, *Journal of Materials Processing Technology*, Vol. 241, 2017, pp. 154-163.

[41] Yang, P., Deibler, L., Bradley, D., Stefan, D., & Carroll, J. Microstructure evolution and thermal properties of an additively manufactured, solution treatable AlSi10Mg part. *Journal of Materials Research*, Vol. 33(23), 2018, pp. 4040-4052.

[42] Baotong Li, Xinxin Yin, Wenhao Tang, Jinhua Zhang, Optimization design of grooved evaporator wick structures in vapor chamber heat spreaders, *Applied Thermal Engineering*, Vol. 166, 2020.

[43] Bailey, C., Thompson, S.M., Derby, M., Morrow, J., Weeks, C., Effect of Build Angle on Additively Manufactured Aluminum Alloy Surface Roughness and Water Wetting Ability, ASME Summer Heat Transfer Conference (SHTC), American Society of Mechanical Engineers, Paper No. HT2021-63599, V001T08A009, 16-18 June, Virtual Event, 2021.

[44] Wiriyasart, Songkran & Naphon, Paisarn. "Fill ratio effects on vapor chamber thermal resistance with different configuration structures." *International Journal of Heat and Mass Transfer*, Vol 127, 2018, pp. 164-171.

Appendix A - Full Drawing Print of Vapor Chamber

The drawing print of the vapor chamber used in this study was too large to fit on any single page. The dimensions most relevant to the study are more clearly shown in Chapter 4.1: Specimen Design and Manufacture, Figures 4.1-4.6. These drawings are to benefit the reader to understand the geometric context of these figures. Because of the context of these features, none of the geometric tolerancing has been defined. Because the vapor chamber at the time of writing has not been cut open to observe the internal surfaces, none of the features have been measured to obtain a reasonable tolerance.

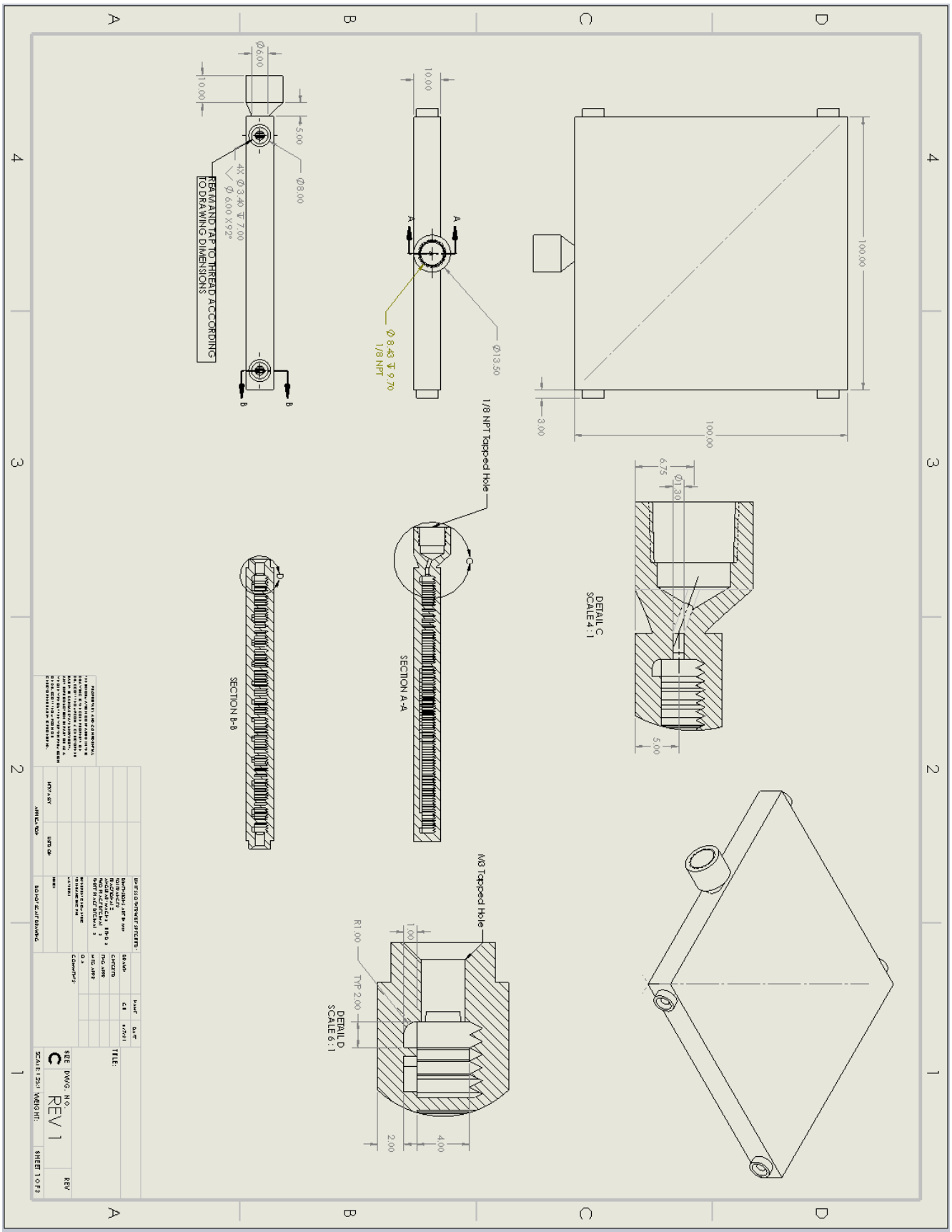
100.00
100.00
3.00
Ø13.50
10.00
Ø 8.43 ↧ 9.70
1/8 NPT
1/8 NPT Tapped Hole
SECTION A-A
Ø6.00
10.00
5.00
Ø8.00
4X Ø 3.40 ↧ 7.00
Ø 6.00 X 92°
REAM AND TAP TO THREAD ACCORDING TO DRAWING DIMENSIONS
SECTION B-B
DETAIL C
SCALE 4 : 1
6.75
Ø1.30
5.00
M3 Tapped Hole
R1.00
1.00
TYP 2.00
DETAIL D
SCALE 6 : 1
2.00
4.00
REV 1
SHEET 1 OF 2

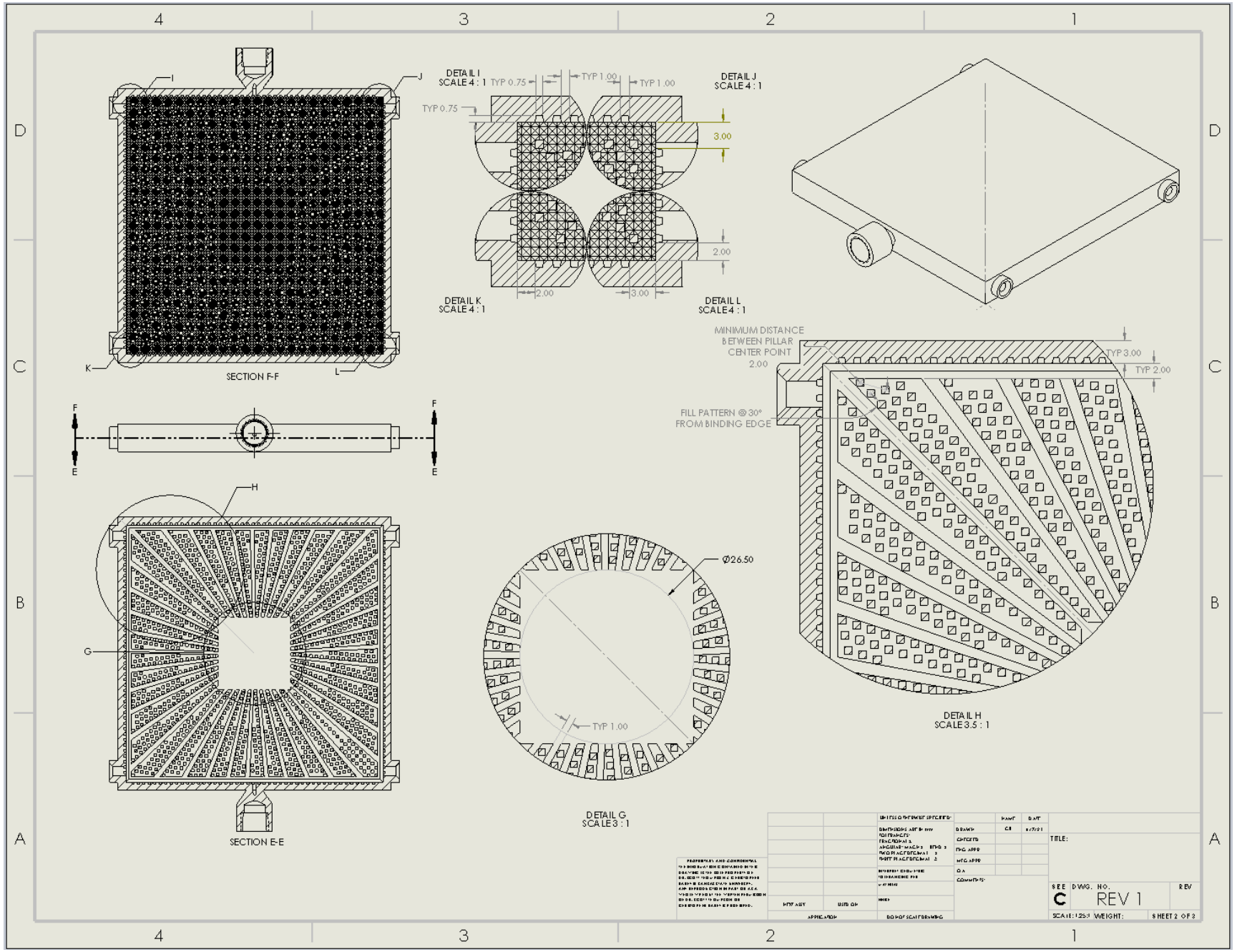
DETAIL I
SCALE 4 : 1
TYP 0.75
TYP 1.00
TYP 1.00
TYP 0.75
3.00
2.00
2.00
3.00
DETAIL J
SCALE 4 : 1
DETAIL K
SCALE 4 : 1
DETAIL L
SCALE 4 : 1
SECTION F-F
SECTION E-E
MINIMUM DISTANCE
BETWEEN PILLAR
CENTER POINT
2.00
TYP 3.00
TYP 2.00
FILL PATTERN @ 30°
FROM BINDING EDGE
DETAIL H
SCALE 3.5 : 1
Ø26.50
TYP 1.00
DETAIL G
SCALE 3 : 1
TITLE:
SIZE
C
DWG. NO.
REV 1
REV
SCALE: 1.25:1
WEIGHT:
SHEET 2 OF 2

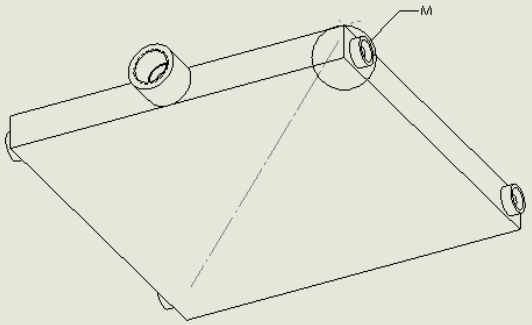

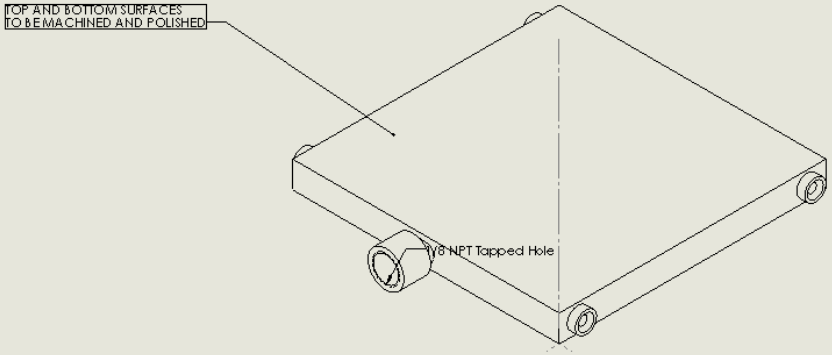

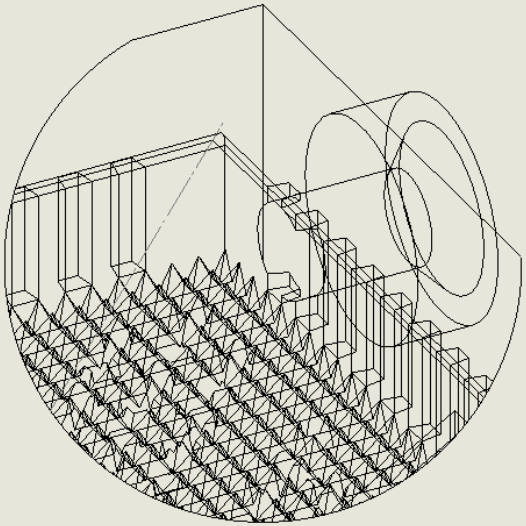

DETAIL M
SCALE 10 : 1

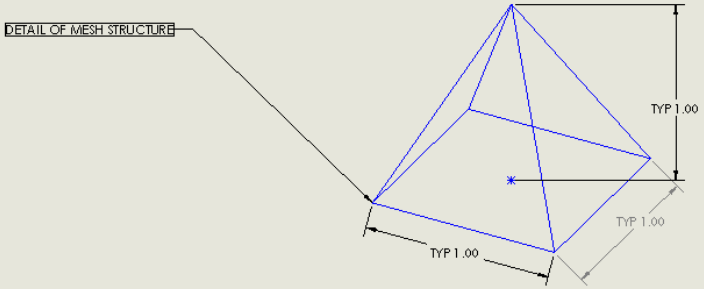

		UNLESS OTHERWISE SPECIFIED:		NAME	DATE
		DIMENSIONS ARE IN mm	DRAWN	CB	6/7/21
		TOLERANCES:	CHECKED		
		FRACTIONAL ±	ENG APPR		
		ANGULAR: MACH ± BEND ±	MFG APPR		
		TWO PLACE DECIMAL ±	Q A		
		THREE PLACE DECIMAL ±	COMMENTS:		
		INTERPRET GEOMETRIC TOLERANCING PER:			
		MATERIAL			
		FINISH			
NEXT ASSY	USED ON				
APPLICATION		DO NOT SCALE DRAWING			

PROPRIETARY AND CONFIDENTIAL
THE INFORMATION CONTAINED IN THIS DRAWING IS THE SOLE PROPERTY OF [illegible]. ANY REPRODUCTION IN PART OR AS A WHOLE WITHOUT THE WRITTEN PERMISSION OF [illegible] IS PROHIBITED.

TITLE:

SIZE	DWG. NO.	REV
C	REV 1	

SCALE: 1:25.1 WEIGHT: SHEET 2 OF 2

Appendix B - National Instruments LABVIEW VI Block Diagram

The block diagram for this program was too large to fit on a single page. The program instructions continue from the first page to the second by connecting in the bottom right and top left corner respectively. Not all the 32 possible thermocouple ports were used which resulted in 7 lines of data which obtained no values. The mean value of each thermocouple was also obtained which does not at this moment in time provide any useful information; however, these will be helpful in the future when studies on transient and steady state temperature values are compared.

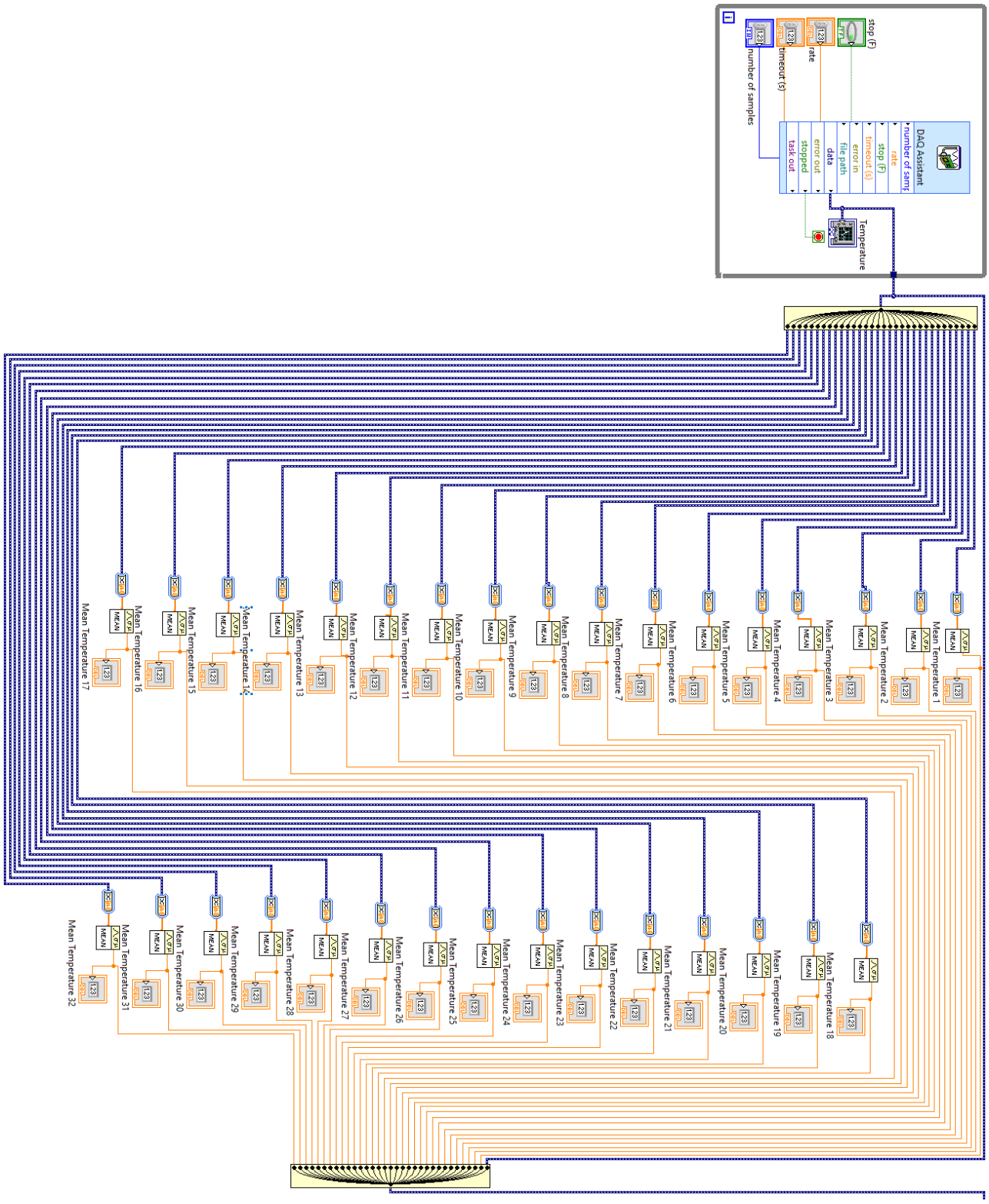
DAQ Assistant
number of samples
rate
stop (F)
timeout (s)
error in
file path
data
error out
stopped
task out
stop (F)
timeout (s)
rate
number of samples
Temperature
Mean Temperature 1
Mean Temperature 2
Mean Temperature 3
Mean Temperature 4
Mean Temperature 5
Mean Temperature 6
Mean Temperature 7
Mean Temperature 8
Mean Temperature 9
Mean Temperature 10
Mean Temperature 11
Mean Temperature 12
Mean Temperature 13
Mean Temperature 14
Mean Temperature 15
Mean Temperature 16
Mean Temperature 17
Mean Temperature 18
Mean Temperature 19
Mean Temperature 20
Mean Temperature 21
Mean Temperature 22
Mean Temperature 23
Mean Temperature 24
Mean Temperature 25
Mean Temperature 26
Mean Temperature 27
Mean Temperature 28
Mean Temperature 29
Mean Temperature 30
Mean Temperature 31
Mean Temperature 32


Set Dynamic Data Attributes
Signals In
Signals Out
Signal Index
Signal Name
Temperature 1
Temperature 2
Temperature 3
Temperature 4
Temperature 5
Temperature 6
Temperature 7
Temperature 8
Temperature 9
Temperature 10
Temperature 11
Temperature 12
Temperature 13
Temperature 14
Temperature 15
Temperature 16
Temperature 17
Temperature 18
Temperature 19
Temperature 20
Temperature 21
Temperature 22
Temperature 23
Temperature 24
Temperature 25
Temperature 26
Temperature 27
Temperature 28
Temperature 29
Temperature 30
Temperature 31
Temperature 32
Mean Temperature 1
Mean Temperature 2
Mean Temperature 3
Mean Temperature 4
Mean Temperature 5
Mean Temperature 6
Mean Temperature 7
Mean Temperature 8
Mean Temperature 9
Mean Temperature 10
Mean Temperature 11
Mean Temperature 12
Mean Temperature 13
Mean Temperature 14
Mean Temperature 15
Mean Temperature 16
Mean Temperature 17
Mean Temperature 18
Mean Temperature 19
Mean Temperature 20
Mean Temperature 21
Mean Temperature 22
Mean Temperature 23
Mean Temperature 24
Mean Temperature 25
Mean Temperature 26
Mean Temperature 27
Mean Temperature 28
Mean Temperature 29
Mean Temperature 30
Mean Temperature 31
Mean Temperature 32
Write To Measurement File
Signals
Flush? (T)
Reset
DAQmx Task
Enable
error in (no error)
Filename
error out
Filename Out
Saving Data
Filename
Enable
Filename Out
Saving Data